PHYSICS OF PLASMAS VOLUME 6, NUMBER 1 JANUARY 1999

Nonlinear δF simulation studies of high-intensity ion beam propagation in a periodic focusing field

Peter H. Stoltz, Ronald C. Davidson, and W. Wei-li Lee
Plasma Physics Laboratory, Princeton University, Princeton, New Jersey 08543

(Received 28 July 1998; accepted 1 October 1998)

This paper makes use of the nonlinear Vlasov–Poisson equations to describe the propagation of an intense, non-neutral ion beam through a periodic focusing solenoidal field with coupling coefficient $\kappa_z(s+S)=\kappa_z(s)$ in the thin-beam approximation $(r_b \ll S)$. The nonlinear δF formalism is developed for numerical simulation applications by dividing the total distribution function F_b into a zero-order part (F_b^0) that propagates through the average focusing field $\overline{\kappa_z}=\text{const}$, plus a perturbation (δF_b) which evolves nonlinearly in the zero-order and perturbed field configurations. To illustrate the application of the technique to axisymmetric, matched-beam propagation, nonlinear δF-simulation results are presented for the case where F_b^0 corresponds to a thermal equilibrium distribution, and the oscillatory component of the coupling coefficient, $\delta\kappa_z(s)=\kappa_z(s)-\overline{\kappa_z}$, turns on adiabatically over many periods S of the focusing lattice. For adiabatic turn-on of $\delta\kappa_z(s)$ over 20–100 lattice periods, the amplitude of the mismatch oscillation is reduced by more than one order of magnitude compared to the case where the field oscillation is turned on suddenly. Quiescent, matched-beam propagation at high beam intensities is demonstrated over several hundred lattice periods. © *1999 American Institute of Physics.* [S1070-664X(99)02401-5]

I. INTRODUCTION AND THEORETICAL MODEL

It is increasingly important to develop an improved theoretical understanding of the equilibrium, stability, and transport properties of intense non-neutral beams propagating in periodic focusing accelerators and transport systems.[1–4] The influence of space-charge effects on nonlinear beam dynamics, stability properties, and halo formation[5–30] is particularly pronounced at the high beam currents and beam densities in the next-generation accelerators envisioned for heavy ion fusion, tritium production, and spallation neutron sources.[31–35] Advanced numerical simulations and analytical studies[13–30] are playing an increasingly critical role in validating theoretical models for comparison with experiment and in the design optimization of next-generation accelerators and beam transport systems. This paper develops the nonlinear δF formalism for intense beam propagation through a periodic solenoidal focusing field,[20–22,36,37] and presents simulation results applying the δF formalism to the case of high-intensity matched-beam propagation over hundreds of lattice periods. Nonlinear δF simulation techniques have been applied successfully to model the nonlinear dynamics and stability properties of magnetically confined fusion plasmas,[38–40] and intense non-neutral beam propagation through a periodic quadrupole lattice,[29,30] and through a uniform focusing solenoidal field.[41] Such δF schemes are found to be attractive in comparison with standard particle-in-cell simulations because they exhibit minimal noise and accuracy problems.

The theoretical model is based on the nonlinear Vlasov–Poisson equations[1,42] and is described in the remainder of Sec. I. In Sec. II, the nonlinear δF formalism is developed for intense beam propagation through a periodic focusing solenoidal field with coupling coefficient $\kappa_z(s+S)=\kappa_z(s)$. The total distribution function F_b is divided into a zero-order part (F_b^0) that propagates through the average focusing field $\overline{\kappa_z}=\text{const}$, plus a perturbation (δF_b) which evolves nonlinearly in the zero-order and perturbed field configurations. To illustrate the application of the technique to axisymmetric, matched-beam propagation, nonlinear δF-simulation results are presented in Sec. III for the case where F_b^0 corresponds to a thermal equilibrium distribution, and the oscillatory component of the coupling coefficient, $\delta\kappa_z(s)=\kappa_z(s)-\overline{\kappa_z}$, turns on adiabatically over many periods S of the focusing lattice. For adiabatic turn-on of $\delta\kappa_z(s)$ over 20–100 lattice periods, the amplitude of the mismatch oscillation is reduced by more than one order of magnitude compared to the case where the field oscillation is turned on suddenly. Quiescent, matched-beam propagation at high beam intensities is demonstrated over several hundred lattice periods.

To summarize the theoretical model, we consider a thin, intense non-neutral ion beam with characteristic radius r_b and axial momentum $\gamma_b m \beta_b c$ propagating in the z direction through a periodic solenoidal focusing field, $\mathbf{B}^{\text{sol}}(\mathbf{x}) = B_z(s)\hat{\mathbf{e}}_z-(r/2)B_z'(s)\hat{\mathbf{e}}_r$, where $B_z(s+S)=B_z(s)$ is the axial field component, s is the axial coordinate, $S=\text{const}$ is the periodicity length, the ''prime'' denotes derivative with respect to s, and $r=(x^2+y^2)^{1/2}$ is the radial distance from the beam axis. Here, we assume a thin beam with $r_b \ll S$ and $\nu = Z_i^2 e^2 N_b/mc^2 \ll \gamma_b$, where ν is Budker's parameter, $\gamma_b mc^2$ is the characteristic energy of a beam particle, $\gamma_b = (1-\beta_b^2)^{-1/2}$ is the relativistic mass factor, $V_b=\beta_b c$ is the axial velocity, c is the speed of light *in vacuo*, and $Z_i e$ and m are the ion charge and rest mass, respectively. The quantity $N_b=\int dx\, dy\, n_b$ is the number of beam particles per unit axial length, where $n_b(x,y,s)$ is the particle density. The thin-beam approximation $(r_b \ll S)$ and the assumption of small Budker's parameter $(\nu \ll \gamma_b)$ are consistent approxima-

Downloaded 30 Aug 2001 to 192.55.106.156. Redistribution subject to AIP license or copyright, see http://ojps.aip.org/pop/popcr.jsp

tions provided the transverse momentum components of a beam particle, p_x and p_y, and the characteristic axial momentum spread, δp_z, are small in comparison with the directed axial momentum $\gamma_b m \beta_b c$, which we assume to be the case. In addition, the present analysis is carried out in the electrostatic approximation, where the self-electric field produced by the beam space-charge is $\mathbf{E}^s = -\nabla \phi^s$, and the electrostatic potential $\phi^s(x,y,s)$ is determined self-consistently from Poisson's equation. Furthermore, to determine the self-magnetic field $\mathbf{B}^s = \nabla \times A_z^s \hat{\mathbf{e}}_z$ produced by the beam current, it is assumed that the axial velocity profile $V_{zb}(x,y,s) \cong \beta_b c$ is approximately uniform over the beam cross section, and the self-magnetic field is approximated by $\mathbf{B}^s = \beta_b \nabla \phi^s \times \hat{\mathbf{e}}_z$.

Consistent with the assumptions described above, the nonlinear δF formalism, developed in Sec. II and applied in Sec. III, makes use of the nonlinear Vlasov–Poisson equations to describe the dynamics of the beam particles and their interaction with the field configuration $\mathbf{E}^s = -\nabla \phi^s$ and $\mathbf{B} = \mathbf{B}^{\mathrm{sol}} + \beta_b \nabla \phi^s \times \hat{\mathbf{e}}_z$. For present purposes, it is convenient to introduce the focusing coefficient $\kappa_z(s+S) = \kappa_z(s)$ and the normalized electrostatic potential $\psi(x,y,s)$ defined by[21,22]

$$\kappa_z(s) = \left(\frac{Z_i e B_z(s)}{2\gamma_b m \beta_b c^2} \right)^2, \qquad \psi(x,y,s) = \frac{Z_i e}{\gamma_b^3 m \beta_b^2 c^2} \, \phi^s(x,y,s). \tag{1}$$

It is also convenient to transform to a frame of reference rotating about the beam axis at the local (normalized) Larmor frequency $\Omega_{\mathrm{L}}(s) = -\sqrt{\kappa_z(s)} = -Z_i e B_z(s)/2\gamma_b m \beta_b c^2$. Introducing the accumulated phase of rotation, $\theta_{\mathrm{L}}(s) = -\int_{s_0}^{s} ds \, \sqrt{\kappa_z(s)}$, the transverse orbits, $X(s)$ and $Y(s)$, in the rotating frame are related to the transverse orbits, $x(s)$ and $y(s)$, in the laboratory frame by $X = x \cos \theta_{\mathrm{L}}(s) + y \sin \theta_{\mathrm{L}}(s)$ and $Y = -x \sin \theta_{\mathrm{L}}(s) + y \cos \theta_{\mathrm{L}}(s)$. Then, assuming that the beam particles have negligibly small axial momentum spread about the average value $\gamma_b m \beta_b c$, it can be shown that the distribution function $F_b(X,Y,X',Y',s)$ evolves according to the nonlinear Vlasov equation[21,22]

$$\frac{\partial F_b}{\partial s} + X' \frac{\partial F_b}{\partial X} + Y' \frac{\partial F_b}{\partial Y} - \left(\kappa_z(s) X + \frac{\partial \psi}{\partial X} \right) \frac{\partial F_b}{\partial X'} - \left(\kappa_z(s) Y + \frac{\partial \psi}{\partial Y} \right) \frac{\partial F_b}{\partial Y'} = 0. \tag{2}$$

Here, $(X,Y,X'Y')$ are phase-space variables appropriate to the Larmor frame, and the normalized potential $\psi(X,Y,s)$ is determined self-consistently from Poisson's equation

$$\left(\frac{\partial^2}{\partial X^2} + \frac{\partial^2}{\partial Y^2} \right) \psi = -\frac{2\pi K}{N_b} \int dX' \, dY' \, F_b. \tag{3}$$

In Eq. (3), $n_b(X,Y,s) = \int dX' \, dY' \, F_b$ is the particle density, $N_b = \int dX \, dY \, n_b$ is the number of particles per unit axial length, and $K = 2N_b Z_i^2 e^2/\gamma_b^3 m \beta_b^2 c^2$ is the self-field perveance. In Eq. (2), note that X' and Y' correspond to normalized velocity variables in the $X-Y$ plane (i.e., X' denotes dX/ds and Y' denotes dY/ds), and the coefficients of $\partial F_b/\partial X'$ and $\partial F_b/\partial Y'$ correspond to the particle accelerations in the X and Y directions, respectively.

The Vlasov–Poisson equations (2) and (3) constitute the basic dynamical equations used in the nonlinear δF formalism in Secs. II and III. They describe, in the Larmor frame, the nonlinear evolution of the charged particle beam as it propagates through the periodic solenoidal field $\kappa_z(s+S) = \kappa_z(s)$. In particular, Eq. (2) describes the incompressible evolution of the distribution function $F_b(X,Y,X',Y',s)$ in the four-dimensional phase space (X,Y,X',Y'), and Eq. (3) determines self-consistently the normalized potential $\psi(X,Y,s)$ in terms of the particle density $n_b(X,Y,s) = \int dX' \, dY' \, F_b$. In subsequent sections, we assume that the $X-Y$ cross section of the beam is enclosed by a perfectly conducting wall (cylindrical or rectangular). Denoting the location of the wall surface by S_w, and the unit vector normal to the wall surface by $\mathbf{n}_w$, Poisson's equation (3) is solved subject to the boundary condition

$$[\mathbf{n}_w \times \nabla \psi] S_w = 0, \tag{4}$$

which corresponds to zero tangential electric field at the conducting wall. In concluding this section, it should also be noted that the characteristics of the nonlinear Vlasov equation (2) correspond to the single-particle equations of motion, e.g., $X'(s) = dX(s)/ds$ and $dX'(s)/ds = -\kappa_z(s) X - \partial\psi/\partial X$ for the X motion, and similar equations for the Y motion.

As a final point regarding the theoretical model, we emphasize that the nonlinear δF formalism developed here is particularly well-suited for application to a periodic focusing solenoidal lattice, $\kappa_z(s) = \overline{\kappa_z} + \delta\kappa_z(s)$, in which case the average lattice coefficient $\overline{\kappa_z} = S^{-1} \int_{s_0}^{s_0+S} ds \, \kappa_z(s)$ is manifestly nonzero [see Eqs. (1) and (31)] and provides transverse confinement of the beam particles making up the equilibrium distribution $F_b^0(H_\perp)$. For adiabatic turn-on of $\delta\kappa_z(s)$, quiescent, highly matched beam propagation at moderate-to-high beam intensity is demonstrated for propagation of a thermal equilibrium beam over hundreds of lattice periods [see, e.g., Figs. 8 and 10 below]. For periodic focusing quadrupole systems, however, it follows that $S^{-1} \int_{s_0}^{s_0+S} ds \, \kappa_q(s) = 0$, and alternative averaging techniques are required to apply the nonlinear δF formalism to high-intensity matched-beam propagation. In this regard, one promising approach for a periodic quadrupole lattice is to first carry out a Floquet transformation[43,44] to incorporate the average effects of the focusing field. This and other approaches are currently under development by the authors for application of the nonlinear δF formalism to periodic quadrupole transport systems.

II. NONLINEAR δF FORMALISM

In Sec. II A, we summarize the nonlinear δF formalism for general periodic focusing lattice $\kappa_z(s+S) = \kappa_z(s)$. Then, for subsequent application, examples of beam equilibrium distributions F_b^0 are presented in Sec. II B for the case of axisymmetric beam propagation through the average focus-

Downloaded 30 Aug 2001 to 192.55.106.156. Redistribution subject to AIP license or copyright, see http://ojps.aip.org/pop/popcr.jsp

ing field $\overline{\kappa_z}=\text{const}$. The dynamics of the root-mean-square beam radius $R_b(s)$ is summarized in Sec. II C.

A. Description of model

For present purposes, the nonlinear Vlasov equation (2) for the distribution function $F_b(X,Y,X',Y',s)$ is expressed in the equivalent form[29,30,41]

$$\frac{d}{ds}F_b=\frac{\partial F_b}{\partial s}+\frac{d\mathbf{X}}{ds}\cdot\frac{\partial F_b}{\partial \mathbf{X}}+\frac{d\mathbf{X}'}{ds}\cdot\frac{\partial F_b}{\partial \mathbf{X}'}=0, \tag{5}$$

where $d\mathbf{X}/ds=X'\hat{\mathbf{e}}_x+Y'\hat{\mathbf{e}}_y$ is the transverse velocity, and

$$\begin{aligned}\frac{d}{ds}X'&=-\kappa_z(s)X-\frac{\partial}{\partial X}\psi,\\ \frac{d}{ds}Y'&=-\kappa_z(s)Y-\frac{\partial}{\partial Y}\psi,\end{aligned} \tag{6}$$

are the transverse acceleration components in Larmor-frame variables. In Eq. (6), $\psi(X,Y,s)$ is determined self-consistently from Poisson's equation (3). In Eq. (5), note that d/ds denotes the *total derivative* with respect to s following the *exact particle motion* in the combined self-fields of the beam and the applied periodic solenoidal field. Therefore, the nonlinear Vlasov equation (5) is simply a statement that the distribution function F_b is constant following the particle motion in the exact field configuration. In the subsequent analysis of Eqs. (5) and (6), we express

$$\kappa_z(s)=\overline{\kappa_z}+\delta\kappa_z(s), \tag{7}$$

where $\delta\kappa_z(s+S)=\delta\kappa_z(s)$ is the oscillatory component of $\kappa_z(s)$, and $\overline{\kappa_z}=\text{const}$ denotes the average value

$$\overline{\kappa_z}=\frac{1}{S}\int_{s_0}^{s_0+S}ds\ \kappa_z(s), \tag{8}$$

where S is the lattice period. Apart from the requirement $\kappa_z(s)\geqslant 0$ [see Eq. (1)], the oscillatory component $\delta\kappa_z(s)$ is allowed to have arbitrary amplitude.

As is customary in the nonlinear δF formalism, we divide the distribution function $F_b(X,Y,X',Y',s)$ into a zero-order part (F_b^0) plus a perturbation (δF_b) according to

$$F_b=F_b^0+\delta F_b\,. \tag{9}$$

Here, $F_b^0(R,X',Y',s)$ is taken to be a known *axisymmetric* solution ($\partial/\partial\Theta=0$) to the nonlinear Vlasov–Poisson equations

$$\frac{\partial F_b^0}{\partial s}+\frac{d\mathbf{X}}{ds}\cdot\frac{\partial F_b^0}{\partial \mathbf{X}}+\left.\frac{d\mathbf{X}'}{ds}\right|_0\cdot\frac{\partial F_b^0}{\partial \mathbf{X}'}=0, \tag{10}$$

$$\frac{1}{R}\frac{\partial}{\partial R}R\frac{\partial\psi^0}{\partial R}=-\frac{2\pi K}{N_b}\int dX'\ dY'\ F_b^0. \tag{11}$$

In Eqs. (10) and (11), $F_b^0(R,X',Y',s)$ and $\psi^0(R,s)$ are assumed to depend on $X=R\cos\Theta$ and $Y=R\sin\Theta$ exclusively through the radial coordinate $R=(X^2+Y^2)^{1/2}$, and the zero-order acceleration components in Eq. (10) are defined by

$$\begin{aligned}\left.\frac{dX'}{ds}\right|_0&=-\overline{\kappa_z}X-\frac{X}{R}\frac{\partial\psi^0}{\partial R},\\ \left.\frac{dY'}{ds}\right|_0&=-\overline{\kappa_z}Y-\frac{Y}{R}\frac{\partial\psi^0}{\partial R}.\end{aligned} \tag{12}$$

With regard to the nonlinear evolution of $\delta F_b(X,Y,X',Y',s)=F_b-F_b^0$, we introduce the weight function $w(X,Y,X',Y',s)$ defined by

$$w=\frac{\delta F_b}{F_b}=1-\frac{F_b^0}{F_b}. \tag{13}$$

It then follows that

$$\frac{dw}{ds}=-\frac{1}{F_b}\frac{dF_b^0}{ds}=-(1-w)\frac{1}{F_b^0}\frac{dF_b^0}{ds}. \tag{14}$$

Here, d/ds is the total derivative following the exact particle motion defined according to Eqs. (5) and (6), and use has been made of $dF_b/ds=0$. Expressing $\psi=\psi^0+\delta\psi$, and making use of $d\mathbf{X}'/ds=d\mathbf{X}'/ds|_0-\delta\kappa_z(s)\mathbf{X}-(\partial/\partial\mathbf{X})\delta\psi$, it readily follows from Eqs. (10) and (14) that

$$\frac{d}{ds}w=(1-w)\left(\delta\kappa_z(s)\mathbf{X}+\frac{\partial}{\partial\mathbf{X}}\delta\psi\right)\cdot\frac{1}{F_b^0}\frac{\partial F_b^0}{\partial\mathbf{X}'}. \tag{15}$$

In Eq. (15), the perturbed potential $\delta\psi(X,Y,s)$ is determined self-consistently in terms of $\delta n_b(X,Y,s)=\int dX'\ dY'\ \delta F_b$ from Poisson's equation

$$\begin{aligned}\left(\frac{\partial^2}{\partial X^2}+\frac{\partial^2}{\partial Y^2}\right)\delta\psi&=-\frac{2\pi K}{N_b}\int dX'\ dY'\ wF_b\\ &=-\frac{2\pi K}{N_b}\int dX'\ dY'\ \frac{w}{1-w}F_b^0.\end{aligned} \tag{16}$$

Here, use has been made of $\delta F_b=wF_b=w(1-w)^{-1}F_b^0$, which follows from Eq. (13).

Equations (15) and (16) for the weight function $w=\delta F_b/F_b$ and the perturbed potential $\delta\psi$, when supplemented by Eqs. (10) and (11) for the zero-order distribution function F_b^0 and self-field potential ψ^0, constitute the final set of dynamical equations in the nonlinear δF formalism, and are fully equivalent to the nonlinear Vlasov–Poisson equations (2) and (3). No *a priori* assumption has been made that δF_b and $\delta\psi$ correspond to small-amplitude perturbations. Of course, the requirements that $F_b^0\geqslant 0$ and $F_b\geqslant 0$, and the definition $w=1-F_b^0/F_b$, lead to the requirement that the weight function w satisfies $w\leqslant 1$. Finally, the nonlinear Vlasov equation (2) of course conserves the number of particles per unit axial length, i.e., $dN_b/ds=(d/ds)\int dX'\ dY\ dX'\times dY'\ F_b=0$. It similarly follows from Eq. (10) that $(d/ds)\int dX'\ dY\ dX'\ dY' F_b^0=0$. Therefore, without loss of generality, we choose to count *all of the particles* in the zero-order distribution function F_b^0, in which case F_b^0 and δF_b are normalized according to

Downloaded 30 Aug 2001 to 192.55.106.156. Redistribution subject to AIP license or copyright, see http://ojps.aip.org/pop/popcr.jsp

$$\begin{aligned}&\int dXdYdX'dY'F_b^0=N_b,\\&\int dXdYdX'dY'\,\delta F_b=0.\end{aligned}\tag{17}$$

That is, the perturbed distribution function $\delta F_b=wF_b$, when averaged over the entire available phase space, occupies equal volumes where $\delta F_b>0(0<w\leqslant 1)$ and $\delta F_b<0(w<0)$.

B. Zero-order equilibrium distribution function F_b^0

The nonlinear δF formalism summarized in Sec. II A has wide applicability to s-dependent periodic solenoidal field configurations with $\kappa_z(s+S)=\kappa_z(s)$. Note from Eqs. (10) and (12) that we have chosen to incorporate the effects of the average focusing field $\overline{\kappa_z}=\mathrm{const}$ in the nonlinear Vlasov equation for F_b^0, whereas the effects of $\delta\kappa_z(s)$ are incorporated in Eq. (15) for the weight function $w=\delta F_b/F_b$. In this case, Eqs. (10) and (11) support a broad range of *equilibrium* solutions $(\partial F_b^0/\partial s=0=\partial\psi^0/\partial s)$ in which the zero-order distribution $F_b^0=F_b^0(H_\perp,P_\Theta)$ depends on the phase-space variables (R,X',Y') exclusively through the single-particle constants of the motion, $H_\perp$ and P_Θ, defined in the Larmor frame by[21,22]

$$\begin{aligned}&H_\perp=\tfrac{1}{2}(X'^2+Y'^2)+\tfrac{1}{2}\overline{\kappa_z}(X^2+Y^2)+\psi^0(R),\\&P_\Theta=XY'-YX'.\end{aligned}\tag{18}$$

Here, the Hamiltonian $H_\perp$ and canonical angular momentum P_Θ are exact single-particle constants of the motion $(dH_\perp/ds=0=dP_\Theta/ds)$ in the equilibrium field configuration because $d\overline{\kappa_z}/ds=0$, and $\partial/\partial\Theta=0$ is assumed in Eqs. (10)–(12). The fact that general distribution function $F_b^0(H_\perp,P_\Theta)$ exactly solves the nonlinear Vlasov–Poisson equations (10) and (11) is readily verified by direct substitution and application of the chain rule for differentiation.

There is clearly enormous latitude[41,42] in specifying the functional form of the zero-order distribution $F_b^0(H_\perp,P_\Theta)$ which serves as the background distribution for the nonlinear δF formalism summarized in Sec. II A and the simulation studies in Sec. III. Once the functional form of $F_b^0(H_\perp,P_\Theta)$ is specified, a wide variety of beam equilibrium properties can be calculated, e.g., the density profile $n_b^0(R)=\int dX'\,dY'\,F_b^0$, the self-field potential $\psi^0(R)$ [Eq. (11)], the average canonical angular momentum $P_{\Theta b}^0(R)=(n_b^0)^{-1}\int dX'\,dY'\,P_\Theta F_b^0$, the transverse temperature profile, etc. In addition, we define the statistical average $\langle\chi\rangle_0$ of a phase function χ over the distribution function $F_b^0(H_\perp,P_\Theta)$ by $\langle\chi\rangle_0=N_b^{-1}\int dX\,dY\,dX'\,dY'\,\chi F_b^0$. For example, the unnormalized beam emittance ϵ_0 and mean-square beam radius R_{b0}^2 associated with the equilibrium distribution F_b^0 are defined in the usual manner by[22]

$$\begin{aligned}&\epsilon_0^2=4\langle X'^2+Y'^2\rangle_0\langle X^2+Y^2\rangle_0,\\&R_{b0}^2=\langle X^2+Y^2\rangle_0.\end{aligned}\tag{19}$$

Here, $dR_{b0}/ds=0=d\epsilon_0/ds$ by virtue of the fact that F_b^0 and ψ^0 correspond to equilibrium solutions with $\partial/\partial s=0$. Without presenting algebraic details, it can be shown that the entire class of distribution functions $F_b^0(H_\perp,P_\Theta)$ solving Eqs. (10) and (11) satisfies the global radial force balance condition[22]

$$\left[\overline{\kappa_z}-\frac{K}{2R_{b0}^2}\right]R_{b0}=\frac{\epsilon_0^2}{4R_{b0}^3}.\tag{20}$$

Equation (20), valid for general choice of $F_b^0(H_\perp,P_\Theta)$, represents a powerful constraint condition on equilibrium beam properties. As expected, Eq. (20) is similar in form to the familiar envelope equation[1,22,36] for the outer radius r_b of a uniform-density Kapchinskij–Vladimirskij (KV) beam equilibrium[5] in the smooth-beam approximation $(dr_b/ds=0)$ provided we make the identification $R_{b0}=r_b/\sqrt{2}$. For specified values of $\overline{\kappa_z}$, K, and ϵ_0^2, note that Eq. (20) can be solved for the mean-square beam radius to give

$$R_{b0}^2=\frac{K}{4\overline{\kappa_z}}+\left[\left(\frac{K}{4\overline{\kappa_z}}\right)^2+\frac{\epsilon_0^2}{4\overline{\kappa_z}}\right]^{1/2}.\tag{21}$$

As expected, note from Eq. (21) that R_{b0}^2 increases with increasing beam intensity (K), increasing beam emittance (ϵ_0), and decreasing solenoidal field strength $(\overline{\kappa_z})$.

In the remainder of Sec. II B, we summarize briefly the equilibrium properties for a few specific choices of distribution function

$$F_b^0=F_b^0(H_\perp)\tag{22}$$

that do not depend explicitly on canonical angular momentum P_Θ. In this case, because $H_\perp$ is an even function of X' and Y' [see Eq. (18)], it follows that there is no average rotation of the beam in the Larmor frame, i.e., $P_{\theta b}^0(R)=(n_b^0)^{-1}\int dX'\,dY'\,P_\Theta F_b^0(H_\perp)=0$, where $P_\Theta=XY'-YX'$.

For future reference, we briefly consider here three specific examples of equilibrium distribution functions $F_b^0(H_\perp)$, ranging from thermal equilibrium [Eq. (23)], to choices of distribution function in which $F_b^0(H_\perp)$ has an *inverted population* in transverse phase-space variables [Eqs. (24) and (25)]. Specifically, we consider the following choices of $F_b^0(H_\perp)$.

Thermal equilibrium:

$$F_b^0(H_\perp)=\hat{n}_b\left(\frac{\gamma_b m\beta_b^2c^2}{2\pi\hat{T}_{\perp b}}\right)\exp\left\{-\frac{\gamma_b m\beta_b^2c^2}{\hat{T}_{\perp b}}H_\perp\right\},\tag{23}$$

Kapchinskij–Vladimirskij (KV) equilibrium:

$$F_b^0(H_\perp)=\frac{\hat{n}_b}{2\pi}\,\delta(H_\perp-\hat{T}_{\perp b}/\gamma_b m\beta_b^2c^2),\tag{24}$$

Gaussian inverted-population (GIP) equilibrium:

$$F_b^0(H_\perp)=\frac{\hat{n}_b}{2\pi}\,\frac{A}{\sqrt{\pi}\Delta}\times\exp\left\{-\frac{(H_\perp-\hat{T}_{\perp b}/\gamma_b m\beta_b^2c^2)^2}{\Delta^2}\right\},\tag{25}$$

where the constant A is defined by

Downloaded 30 Aug 2001 to 192.55.106.156. Redistribution subject to AIP license or copyright, see http://ojps.aip.org/pop/popcr.jsp

TABLE I. Equilibrium properties for various choices of $F_b^0(H_\perp)$.

Distribution function $F_b^0(H_\perp)$	Density profile $n_b^0(R)$	Temperature profile $T_{\perp b}^0(R)$	Transverse emittance ϵ_0^2
(1) Thermal equilibrium in Eq. (23)	$\hat{n}_b \exp\left\{-\frac{\gamma_b m\beta_b^2c^2}{2\hat{T}_{\perp b}}[\overline{\kappa_z}R^2+2\psi^0]\right\}$	$\hat{T}_{\perp b}=\text{const}$	$\frac{8\hat{T}_{\perp b}}{\gamma_b m\beta_b^2c^2}R_{b0}^2$
(2) KV distribution in Eq. (24)	$\hat{n}_b=\text{const}$ for $0\leqslant R<r_b\equiv\sqrt{2}R_{b0}$; (zero, otherwise)	$\hat{T}_{\perp b}\left(1-\frac{R^2}{r_b^2}\right)$ for $0\leqslant R<r_b\equiv\sqrt{2}R_{b0}$; (zero, otherwise)	$\frac{4\hat{T}_{\perp b}}{\gamma_b m\beta_b^2c^2}R_{b0}^2$
(3) Gaussian IP distribution in Eq. (25)	$\hat{n}_b\frac{A}{\sqrt{\pi}\Delta}\int_{-V(R)}^{\infty}dU\exp\left(-\frac{U^2}{\Delta^2}\right)$	$\gamma_b m\beta_b^2c^2\left[V(R)+\frac{\hat{n}_bA\Delta}{2\sqrt{\pi}}\frac{\exp(-V^2/\Delta^2)}{n_b^0(R)}\right]$	Determine from Eq. (19)

$$A\equiv\left[\frac{1}{\sqrt{\pi}\Delta}\int_{-\hat{T}_{\perp b}/\gamma_b m\beta_b^2c^2}^{\infty}dU\,\exp(-U^2/\Delta^2)\right]^{-1}.$$

Here, $\hat{n}_b$ and $\hat{T}_{\perp b}$ are positive constants with dimensions of density and temperature (energy units), respectively, $H_\perp$ is the (dimensionless) Hamiltonian defined in Eq. (18), and Δ is a positive, dimensionless constant. Without loss of generality, we take the on-axis self-field potential to be $\psi^0(R=0)=0$, and identify $\hat{n}_b=n_b^0(R=0)$ with the on-axis beam density. For each choice of $F_b^0(H_\perp)$ in Eqs. (23)–(25), the normalized electrostatic potential $\psi^0(R)$, is determined self-consistently in terms of the beam density $n_b^0(R)=\int dX'\,dY'\,F_b^0(H_\perp)$ from the equilibrium Poisson equation (11). Finally, for the general class of beam equilibria $F_b^0(H_\perp)$, the transverse temperature profile is defined in dimensional energy units by[21]

$$n_b^0(R)T_{\perp b}^0(R)=\frac{1}{2}\gamma_b m\beta_b^2c^2\int dX'\,dY'\times(X'^2+Y'^2)F_b^0(H_\perp),\tag{26}$$

where $n_b^0(R)=\int dX'\,dY'\,F_b^0(H_\perp)$.

A detailed evaluation of beam equilibrium properties for the choice of distribution functions in Eqs. (23)–(25) is presented elsewhere,[21] and essential results are summarized in Table I. Here, for the Gaussian inverted-population (GIP) distribution in Eq. (25) and Table I, the effective potential $V(R)$ is defined by

$$V(R)=\frac{\hat{T}_{\perp b}}{\gamma_b m\beta_b^2c^2}-\frac{1}{2}\overline{\kappa_z}R^2-\psi^0(R).\tag{27}$$

In the limit $\Delta\rightarrow 0_+$, note that $A\rightarrow 1$ and the Gaussian distribution in Eq. (25) reduces exactly to the (singular) KV distribution in Eq. (24), because of the identity $\lim_{\Delta\rightarrow 0_+}(\sqrt{\pi}\Delta)^{-1}\exp[-(U-V)^2/\Delta^2]=\delta(U-V)$. In general, for each choice of $F_b^0(H_\perp)$ in Eqs. (23)–(25), the mean-square beam radius R_{b0}^2 is related to the self-field perveance $K=2N_bZ_i^2e^2/\gamma_b^3m\beta_b^2c^2$, the average focusing coefficient $\overline{\kappa_z}$, and the unnormalized beam emittance ϵ_0 by the radial force-balance equation (20), or equivalently, Eq. (21). Furthermore, the necessary condition for the existence of radially confined equilibrium solutions with $n_b^0(R\rightarrow\infty)=0$ can be expressed as[21,42]

$$\delta\equiv\frac{\overline{\kappa_z}\beta_b^2c^2}{\hat{\omega}_{pb}^2/2\gamma_b^2}-1>0.\tag{28}$$

Here, $\hat{\omega}_{pb}^2=4\pi Z_i^2e^2\hat{n}_b/\gamma_b m$ is the on-axis plasma frequency-squared. Equation (28) is simply a statement that the magnetic focusing force (as measured by $\overline{\kappa_z}\beta_b^2c^2$) must exceed the net repulsive self-field force (as measured by $\hat{\omega}_{pb}^2/2\gamma_b^2$) for existence of radially confined equilibria. For the choice of distribution functions in Eqs. (23) and (25), we note from Table I that the formal expressions for the density profile $n_b^0(R)$ depend explicitly on $\psi^0(R)$, and the (highly nonlinear) Poisson's equation (11) for $\psi^0(R)$ must be solved numerically. As a general remark, whenever the dimensionless parameter δ is sufficiently small in comparison with unity, the density profile $n_b^0(R)$ calculated numerically from Eq. (11) and Table I is found to be radially very broad in units of the thermal Debye length. For example, for the thermal equilibrium distribution in Eq. (23), whenever $\delta\ll 1$ is sufficiently small, it is found that the rms beam radius R_{b0} is much larger than the thermal Debye length $\lambda_D=(\gamma_b^2\hat{T}_{\perp b}/4\pi\hat{n}_bZ_i^2e^2)^{1/2}$, with $n_b^0(R)\simeq\hat{n}_b=\text{const}$, in the beam interior, and $n_b^0(R)$ dropping rapidly to exponentially small values over a few Debye lengths at the beam surface.[21,42] For the specific choice of thermal equilibrium distribution $F_b^0(H_\perp)$ in Eq. (23), typical numerical solutions for the radial density profile $n_b^0(R)=\int dX'\,dY'\,F_b^0(H_\perp)$ obtained from the nonlinear Poisson equation (11) are illustrated in Fig. 1. Here, we have introduced an equivalent lattice period S_{eq} defined by $S_{\text{eq}}=1/\sqrt{\overline{\kappa_z}}$, and Fig. 1 shows plots of normalized density $n_b^0(R)/\hat{n}_b$ vs R/S_{eq} for several values of the dimensionless parameter $KS_{\text{eq}}/\epsilon_0$ obtained at fixed value of beam current (as measured by K), and decreasing values of beam emittance $\epsilon_0=[(8\hat{T}_{\perp b}/\gamma_b m\beta_b^2c^2)R_{b0}^2]^{1/2}$. As expected, we note from Fig. 1 that the shape of the density profile $n_b^0(R)$ varies from diffuse and bell-shaped for $KS_{\text{eq}}/\epsilon_0=0.5$, to a density profile with relatively sharp radial boundary for $KS_{\text{eq}}/\epsilon_0=5$.

From Table I, there are interesting similarities and differences in the equilibrium properties calculated for the distribution functions in Eqs. (23)–(25). For example, both Eq. (23) and Eq. (25) lead to bell-shaped density profiles with maximum density ($\hat{n}_b$) occurring on axis ($R=0$). By con-

Downloaded 30 Aug 2001 to 192.55.106.156. Redistribution subject to AIP license or copyright, see http://ojps.aip.org/pop/popcr.jsp

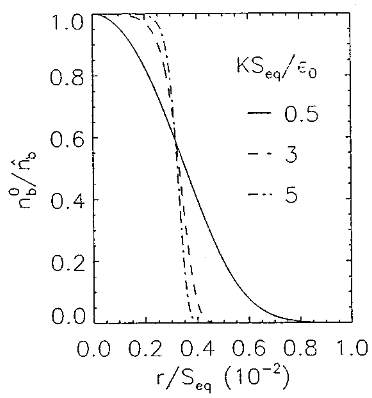

FIG. 1. Plot of normalized density profile $n_b^0(R)/\hat{n}_b$ vs R/S_{eq} obtained numerically from Eq. (11) for the choice of thermal equilibrium distribution $F_b^0(H_\perp)$ in Eq. (23) and several values of dimensionless beam intensity corresponding to $KS_{\text{eq}}/\epsilon_0=0.5,3,5$. Here, $S_{\text{eq}}\equiv 1/\sqrt{\overline{\kappa_z}}$.

trast, the KV distribution in Eq. (24) has a uniform density profile, with $n_b^0(R)=\hat{n}_b=\text{const}$ over the interval $0\leqslant R<r_b$, and $n_b^0(R)=0$ for $r>r_b$. Here, the outer beam radius r_b is determined from the condition $\psi^0(r_b)+(1/2)\overline{\kappa_z}r_b^2=\hat{T}_{\perp b}/\gamma_b m\beta_b^2c^2$, where $\psi^0(R)=-(1/2)KR^2/r_b^2$ in the beam interior $(0\leqslant R<r_b)$. Furthermore, from Table I, the transverse temperature profile $T_{\perp b}^0(R)$ is uniform (and equal to $\hat{T}_{\perp b}=\text{const}$) for the thermal equilibrium distribution in Eq. (23), whereas $T_{\perp b}^0(R)$ decreases as a function of R for the inverted-population distributions in Eqs. (24) and (25).

The Gaussian inverted-population distribution in Eq. (25) is particularly interesting. As noted earlier, in the limit $\Delta\to 0_+$, Eq. (25) reduces identically to the KV beam equilibrium[5] in Eq. (24). Furthermore, from Eq. (27) and Table I, because $V(R=0)=\hat{T}_{\perp b}/\gamma_b m\beta_b^2c^2$ and $V(R\to\infty)=-\infty$, it follows that $n_b^0(R=0)=\hat{n}_b$, and the density $n_b^0(R)$ decreases monotonically with increasing R, with $n_b^0(R\to\infty)=0$. In the limit $\Delta\to 0_+$, the density profile $n_b^0(R)$ corresponding to Eq. (25) of course reduces to the step-function profile in Table I for the KV distribution. An appealing feature of the Gaussian inverted-population distribution in Eq. (25) relative to the KV distribution in Eq. (24) is the fact that the velocity derivative factor, $F_b^{0^{-1}}\partial F_b^0/\partial \mathbf{X}'$, which occurs in Eq. (15) for the weight function w, is not a singular function for the case of the Gaussian inverted-population distribution (when $\Delta\neq 0$), whereas it is a singular function for the case of a KV distribution. Nonetheless, Eq. (25) does enjoy some similarity in features to Eq. (24), e.g., an inverted population in phase space. By contrast, the thermal equilibrium distribution in Eq. (23) is a monotonic decreasing function of $H_\perp$ with $\partial F_b^0/\partial H_\perp\leqslant 0$. We therefore expect the stability properties of the equilibrium distribution in Eq. (23) to differ from the stability properties of the equilibrium distributions in Eqs. (24) and (25), which have inverted populations in $H_\perp$.[42] Although nonlinear δF-simulation results for high-intensity matched-beam propagation are presented in Sec. III only for the case of the thermal equilibrium distribution $F_b^0(H_\perp)$ in Eq. (23), we have summarized above and in Table I equilibrium properties for the two other choices of distribution functions in Eqs. (24) and (25) for reference in future nonlinear δF-simulation studies.

C. Dynamics of root-mean-square beam radius $R_b(s)$

An important diagnostic tool in the nonlinear δF-simulation studies in Sec. III will be to monitor the dynamics of the rms beam radius $R_b(s)$ defined by $R_b^2(s)=\langle X^2+Y^2\rangle$. For axisymmetric beam propagation $(\partial/\partial\Theta=0)$, an *exact* consequence of the nonlinear Vlasov–Poisson equations (2) and (3) is that the rms beam radius $R_b(s)$ evolves according to[22]

$$\frac{d^2}{ds^2}R_b(s)+\left[\kappa_z(s)-\frac{K}{2R_b^2(s)}\right]R_b(s)=\frac{\epsilon^2(s)}{4R_b^3(s)}. \tag{29}$$

Here, $\kappa_z(s)=\overline{\kappa_z}+\delta\kappa_z(s)$ is the s-dependent focusing coefficient, statistical averages over the distribution function $F_b(X,Y,X',Y',s)$ are defined by $\langle\chi\rangle=N_b^{-1}\int dX\,dY\,dX'\,dY'\,\chi F_b$, and the unnormalized beam emittance $\epsilon(s)$ is defined by

$$\epsilon^2(s)=4[\langle X'^2+Y'^2\rangle\langle X^2+Y^2\rangle-\langle XX'+YY'\rangle^2]. \tag{30}$$

For the special case of a uniform focusing field with $\delta\kappa_z(s)=0$ and $\kappa_z(s)=\overline{\kappa_z}=\text{const}$, and constant values of rms beam radius R_{b0} and emittance ϵ_0, Eq. (29) reduces to the radial force balance condition in Eq. (20), as expected.

For application in the numerical simulations in Sec. III, we consider a fully developed periodic focusing field $\kappa_z(s+S)=\kappa_z(s)$ in which the axial field has a sinusoidal component with $B_z(s)=B_{z0}[1+(\Delta_m/2)\cos(2\pi s/S)]$, where B_{z0}, Δ_m, and S are constants. Thus, $\kappa_z(s)=[Z_ieB_z(s)/2\gamma_b m\beta_b c^2]^2=\overline{\kappa_z}+\delta\kappa_z(s)$, where

$$\begin{aligned}\overline{\kappa_z}&=\kappa_{z0}(1+\Delta_m^2/8),\\ \delta\kappa_z(s)&=\overline{\kappa_z}\left[\frac{\Delta_m}{1+\Delta_m^2/8}\cos\left(\frac{2\pi s}{S}\right)\right.\\ &\qquad\left.+\frac{\Delta_m^2/8}{1+\Delta_m^2/8}\cos\left(2\cdot\frac{2\pi s}{S}\right)\right],\end{aligned} \tag{31}$$

and $\kappa_{z0}\equiv(Z_ieB_{z0}/2\gamma_b m\beta_b c^2)^2$.

The nonlinear equation (29) for the rms beam radius $R_b(s)$ can be integrated numerically[22] for a wide range of system parameters and choices of periodic lattice function $\kappa_z(s+S)=\kappa_z(s)$. For the special case of *small-amplitude* oscillations about the average beam radius R_{b0} defined in Eqs. (20) and (21), we express $R_b(s)=R_{b0}+\delta R_b(s)$, and linearize Eq. (29). Treating $\epsilon^2\simeq\epsilon_0^2=\text{const}$, and approximating $\delta\kappa_z(s)=\overline{\kappa_z}\Delta_m\cos(2\pi s/S)$ for small values of $\Delta_m^2/8\ll 1$, this gives

$$\frac{d^2}{ds^2}\delta R_b(s)+k_e^2\delta R_b(s)=-\overline{\kappa_z}\Delta_m\,R_{b0}\cos(k_s s), \tag{32}$$

where $k_s\equiv 2\pi/S$, and the envelope-oscillation wave number k_e is defined by

Downloaded 30 Aug 2001 to 192.55.106.156. Redistribution subject to AIP license or copyright, see http://ojps.aip.org/pop/popcr.jsp

$$k_e^2 \equiv \overline{\kappa_z}\left[1+\frac{K}{2\overline{\kappa_z}R_{b0}^2}+\frac{3\epsilon_0^2}{4\overline{\kappa_z}R_{b0}^4}\right]$$
$$=4\overline{\kappa_z}\,\frac{[(KS/\epsilon_0)^2+4\overline{\kappa_z}S^2]^{1/2}}{KS/\epsilon_0+[(KS/\epsilon_0)^2+4\overline{\kappa_z}S^2]^{1/2}}. \qquad (33)$$

From Eq. (33), we note that the envelope-oscillation wave number k_e varies from $k_e^2=4\overline{\kappa_z}$ for a low-intensity beam $(K/\epsilon_0\sqrt{\overline{\kappa_z}}\ll 1)$ to $k_e^2=2\overline{\kappa_z}$ for a high-intensity beam $(K/\epsilon_0\sqrt{\overline{\kappa_z}}\gg 1)$. Furthermore, the general solution to Eq. (32) is

$$\delta R_b(s)=\frac{R_{b0}\overline{\kappa_z}\Delta_m}{k_s^2-k_e^2}\,[\cos(k_s s)-\cos(k_e s)]$$
$$+\delta R_b(0)\cos(k_e s)+\frac{1}{k_e}\,\delta R_b'(0)\sin(k_e s), \qquad (34)$$

where $\delta R_b(0)$ and $\delta R_b'(0)$ are the initial values at $s=0$. It is evident from Eq. (34) that $\delta R_b(s)$ generally has oscillatory components at wavelength $\lambda_e=2\pi/k_e$, and at wavelength $\lambda_s=2\pi/k_s=S$ corresponding to the period of the applied focusing field. Only for the special initial conditions with

$$\delta R_b'(0)=0,$$
$$\delta R_b(0)=\overline{\kappa_z}\Delta_m R_{b0}/(k_s^2-k_e^2), \qquad (35)$$

is the beam truly *matched*, with $\delta R_b(s)$ oscillating only at the period $S=2\pi/k_s$ of the focusing field [the first term on the right-hand side of Eq. (34)].

In the present paper, we make use of Eq. (29), in particular the linearized version in Eq. (32), as a *diagnostic tool* to infer the natural wavelength components making up $\delta R_b(s)=R_b(s)-R_{b0}$, and to compare with the fast Fourier transform of $\delta R_b(s)$ measured in the δF simulations [see Eq. (41)]. The envelope oscillation wave number k_e [Eqs. (33) and (34)] of course includes the effects of the (depressed) betatron oscillations of the beam ions. Consistent (for example) with the application in Ref. 37, we take $|\delta\kappa_z(s)|\lesssim 0.2$ in the present simulations. In this case it is found that $|\delta R_b/R_{b0}|\lesssim 1-5\times 10^{-3}$, and the linearization approximation in Eq. (32) is fully adequate for identifying the key wavelength components of $\delta R_b(s)$.

In the simulations presented in Sec. III, we will find that both frequency components in Eq. (34) are generally present in $\delta R_b(s)$ for the case where $\delta\kappa_z(s)$ in Eq. (31) is *turned on suddenly* at $s=0$. As a second approach, we adopt an *adiabatic turn-on model* in which $B_z(s)=B_{z0}[1+(1/2)\Delta(s)\cos(k_s s)]$, where (for example) the coefficient $\Delta(s)$ is defined by

$$\Delta(s)=\Delta_m\left[1-\exp\left(-\alpha\,\frac{s}{S}\right)\right], \qquad (36)$$

where α is a positive constant. For $s=0$, Eq. (36) reduces to $\Delta=0$, and for $s\gg\alpha^{-1}S$, $\Delta(s)$ asymptotes at $\Delta_m=\text{const}$. That is, using Eq. (36) with sufficiently small value of α, $\delta\kappa_z(s)$ turns on adiabatically over many lattice periods, and achieves the constant-amplitude oscillatory form in Eq. (31) for $s\gg\alpha^{-1}S$. In this case, it is found in the nonlinear δF simulations presented in Sec. III that *matched-beam* solutions are readily obtained with $\delta R_b(s)$ oscillating with the same period S as the periodic focusing field.

III. NONLINEAR δF SIMULATION STUDIES

In this section, we present the equations followed in the nonlinear δF simulations, discuss initial conditions and conservation properties, and present numerical results for several choices of the adiabatic turn-on parameter α, and dimensionless self-field parameter KS/ϵ_0. All simulations presented here corresponds to the case where $F_b^0(H_\perp)$ is chosen to be the thermal equilibrium distribution in Eq. (23) (see also Fig. 1), although the δF formalism is readily applied to other choices of $F_b^0(H_\perp)$. The main result of this section is that adiabatic turn-on of $\delta\kappa_z(s)$ with sufficiently small value of α leads to matched-beam solutions that can propagate quiescently over several hundred lattice periods. By contrast, sudden turn-on of $\delta\kappa_z(s)$ leads to strong beam mismatch in which $\delta R_b(s)=R_b(s)-R_{b0}$ has oscillatory components at wavelengths $\lambda_e=2\pi/k_e$ and $\lambda_s=2\pi/k_s=S$ [see Eq. (34)].

The δF simulations follow the particle trajectories and weights as functions of s. One can derive the necessary equations using the Klimontovich representation for the distribution function[1]

$$F_b=\frac{N_b}{N_p}\sum_{i=1}^{N_p}\delta(\mathbf{X}-\mathbf{X}_i)\,\delta(\mathbf{X}'-\mathbf{X}_i'), \qquad (37)$$

where N_p is the number of particles used in the simulations, and $N_b=\int dX\,dY\,dX'\,dY'\,F_b$ is the number of particles per unit length. For this representation of F_b, assuming per-

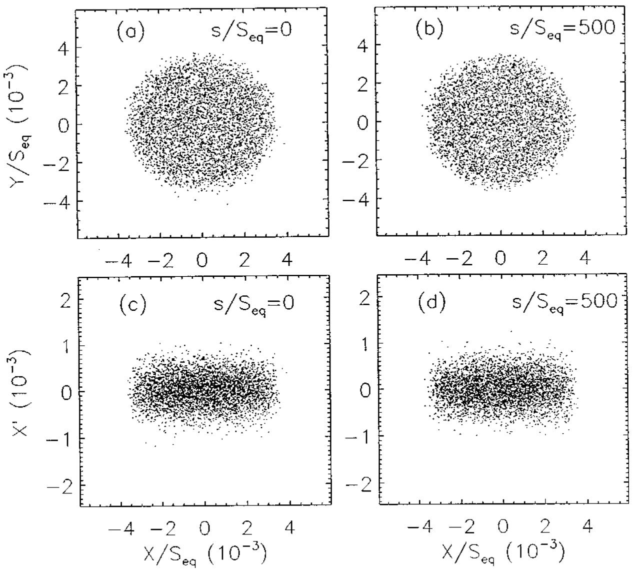

FIG. 2. Phase-space plots corresponding to (X,Y) at (a) $s=0$ and (b) $s=500\,S_{\text{eq}}$, and (X,X') at (c) $s=0$ and (d) $s=500\,S_{\text{eq}}$. System parameters correspond to a thermal equilibrium beam with $KS_{\text{eq}}/\epsilon_0=7$ propagating through a uniform focusing field with $\delta\kappa_z(s)=0$. Other parameters for this simulation correspond to $N_p=10{,}000$ particles, 512 radial grid points, and time step $\Delta s=0.01\,S_{\text{eq}}$.

Downloaded 30 Aug 2001 to 192.55.106.156. Redistribution subject to AIP license or copyright, see http://ojps.aip.org/pop/popcr.jsp

turbations about the thermal equilibrium distribution $F_b^0(H_\perp)$ in Eq. (23), the equations for $\mathbf{X}_i(s)$ and $w_i(s)$ reduce to [see Eqs. (6) and (15)]

$$\mathbf{X}_i'' = -[\overline{\kappa_z} + \delta\kappa_z(s)]\mathbf{X}_i - \left(\frac{\partial}{\partial \mathbf{X}_i} \psi_0(\mathbf{X}_i) + \frac{\partial}{\partial \mathbf{X}_i} \delta\psi(\mathbf{X}_i, s) \right), \tag{38}$$

$$w_i' = -(1 - w_i)\left[\delta\kappa_z(s)\mathbf{X}_i + \frac{\partial}{\partial \mathbf{X}_i} \delta\psi(\mathbf{X}_i, s) \right] \cdot \frac{\gamma_b m \beta_b^2 c^2}{\hat{T}_{\perp b}} \mathbf{X}_i' . \tag{39}$$

For the simulations presented here, we assume an axisymmetric beam ($\partial/\partial\Theta = 0$), and use Eqs. (16), (37), and $\delta F_b = wF_b$ to write

$$\frac{\partial}{\partial R} \delta\psi(R, s) = -\frac{K}{RN_p} \sum_{R_i < R}^{N_p} w_i(\mathbf{X}_i, s), \tag{40}$$

where $R^2 = X^2 + Y^2$.

From the analysis in Sec. II C, the rms beam radius $R_b(s)$ is expected to oscillate at two distinct frequencies. Hence, we monitor the change in $R_b^2(s)$, calculated from

$$\begin{aligned}
\delta R_b^2(s) &= \delta\langle X^2 + Y^2 \rangle \\
&= \langle X^2 + Y^2 \rangle - \langle X^2 + Y^2 \rangle_0 \\
&= \frac{1}{N_b} \int (X^2 + Y^2)(F_b - F_b^0) dX\, dY\, dX'\, dY' \\
&= \frac{1}{N_b} \int (X^2 + Y^2) wF_b\, dX\, dY\, dX'\, dY' \\
&= \frac{1}{N_p} \sum_{i=1}^{N_p} w_i (X_i^2 + Y_i^2).
\end{aligned} \tag{41}$$

Similarly, from Eqs. (30), (37), and $\delta F_b = wF_b$, we monitor the change in emittance-squared calculated from

$$\begin{aligned}
\delta\epsilon^2(s) &= \epsilon^2(s) - \epsilon_0^2 \\
&= \frac{4}{N_p^2} \Bigg[\left(\sum_{i=1}^{N_p} w_i (X_i'^2 + Y_i'^2) \right) \left(\sum_{i=1}^{N_p} w_i (X_i^2 + Y_i^2) \right) \\
&\quad + N_p R_{b0}^2 \sum_{i=1}^{N_p} w_i (X_i'^2 + Y_i'^2) \\
&\quad + \frac{1}{4} N_p \epsilon_0^2 \sum_{i=1}^{N_p} w_i (X_i^2 + Y_i^2) \\
&\quad - \left(\sum_{i=1}^{N_p} w_i (X_i X_i' + Y_i Y_i') \right)^2 \Bigg].
\end{aligned} \tag{42}$$

Simulation results are presented in this section for the case where $B_z(s) = B_{z0}[1 + (1/2)\Delta(s)\cos(2\pi s/S)]$ and $\Delta(s)$ is defined in Eq. (36). For $\alpha = \infty$ (sudden turn-on), $\delta\kappa_z(s)$ turns on abruptly to the wave form in Eq. (31). On the other hand, for $\alpha \ll 1$ (adiabatic turn-on), $\delta\kappa_z(s)$ turns on slowly and achieves the wave form in Eq. (31) for $s \gg S/\alpha$. In this section, we present simulation results for the case where $\sqrt{\overline{\kappa_z}}S = 1$, corresponding to $S = S_{\mathrm{eq}} = 1/\sqrt{\overline{\kappa_z}}$. It is also convenient to define an effective phase advance σ by $\sigma \equiv \epsilon_0 S/2R_{b0}^2$, where R_{b0}^2 is the equilibrium mean-square radius defined in Eq. (21). Therefore, for $\sqrt{\overline{\kappa_z}}S = 1$, it follows that the vacuum phase advance $\sigma_v \equiv \lim_{K\to 0} \sigma$ is $\sigma_v = 57.3°$. From Eq. (21) and $\sigma = \epsilon_0 S/2R_{b0}^2$, it then follows that the *depressed* phase advance (including space-charge effects) is $\sigma = 44.7°$ and $\sigma = 11°$ for the two cases $KS/\epsilon_0 = 0.5$ and $KS/\epsilon_0 = 5$, respectively. In the simulations presented in this section, unless otherwise indicated, we take $\Delta_m = 0.2$ as suggested in Ref. 37, and the simulations are carried out with $N_p = 20\,000$ particles, 1024 radial grid points, and time steps of $\Delta s/S = 0.001$.

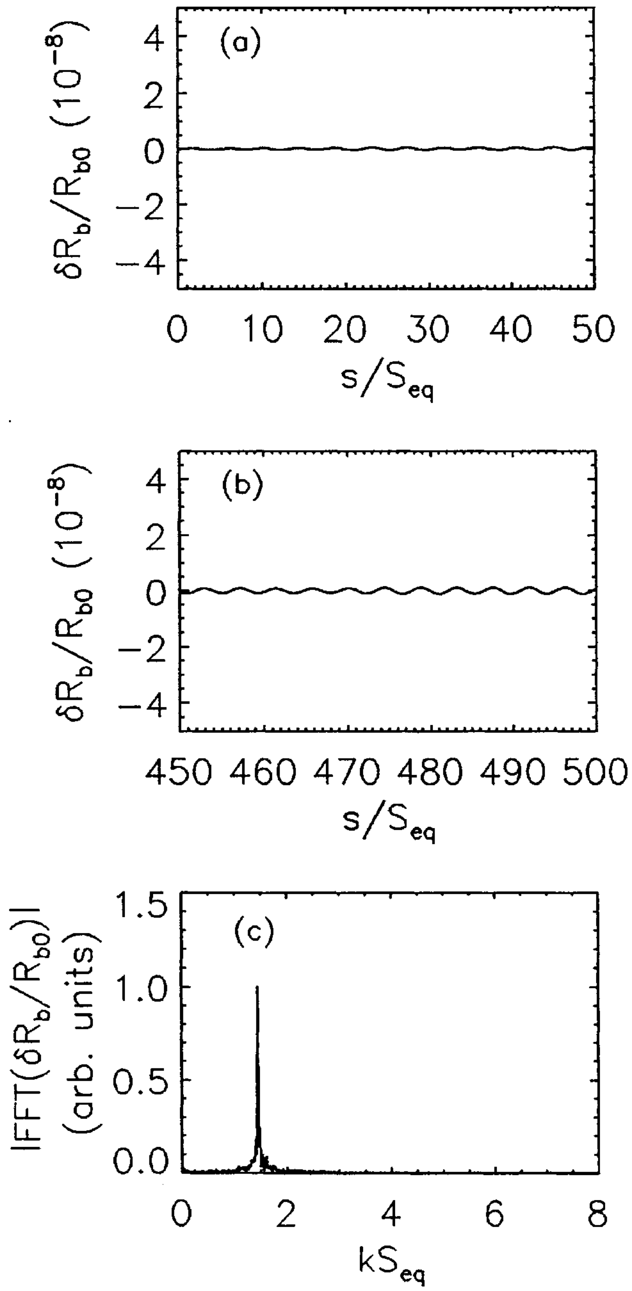

FIG. 3. Plots of variation in rms beam radius $\delta R_b(s)$ vs s determined numerically from Eq. (40) over the intervals (a) $s = 0$ to $s = 50\, S_{\mathrm{eq}}$, and (b) $s = 450\, S_{\mathrm{eq}} = s = 500\, S_{\mathrm{eq}}$. (c) shows a plot of the fast-Fourier transform of $\delta R_b(s)$ integrated over the interval $s = 0$ to $s = 500\, S_{\mathrm{eq}}$. System parameters are identical to those in Fig. 2.

Downloaded 30 Aug 2001 to 192.55.106.156. Redistribution subject to AIP license or copyright, see http://ojps.aip.org/pop/popcr.jsp

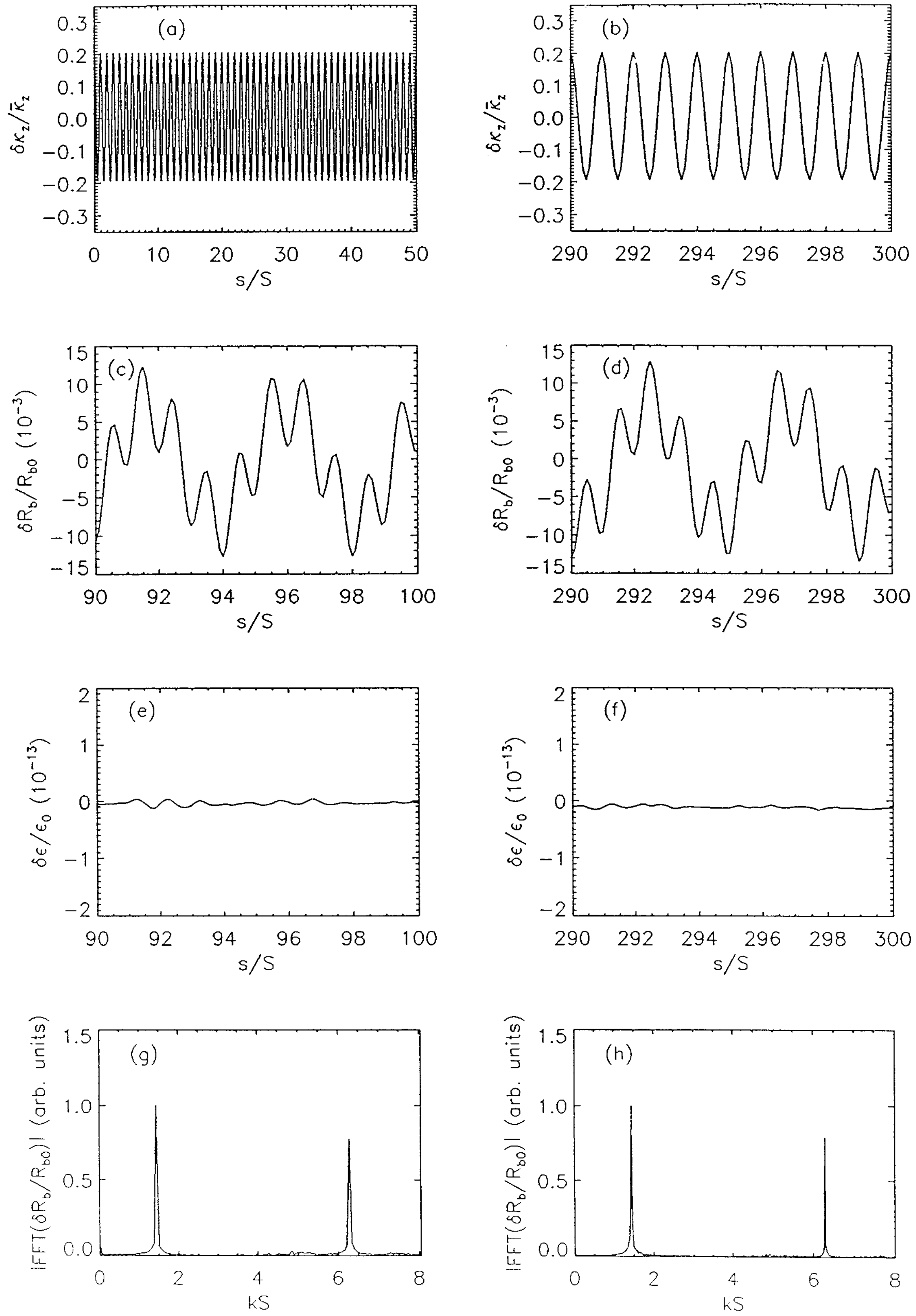

FIG. 4. Nonlinear δF-simulation results for sudden turn-on of $\delta\kappa_z(s)$ with $\alpha=\infty$ and $\Delta_m=0.2$, and normalized beam intensity $KS/\epsilon_0=5$. Beam propagation is from $s=0$ to $s=300\ S$, and perturbations are about the thermal equilibrium distribution $F_b^0(H_\perp)$ in Eq. (23). Shown are plots vs s/S of (a) $\delta\kappa_z(s)/\bar{\kappa}_z$ from $s=0$ to $s=50\ S$; (b) $\delta\kappa_z(s)/\bar{\kappa}_z$ from $s=290\ S$ to $s=300\ S$; (c) $\delta R_b(s)/R_{b0}$ from $s=90\ S$ to $s=100\ S$; (d) $\delta R_b(s)/R_{b0}$ from $s=290\ S$ to $s=300\ S$; (e) $\delta\epsilon(s)/\epsilon_0$ from $s=90\ S$ to $s=100\ S$; and (f) $\delta\epsilon(s)/\epsilon_0$ from $s=290\ S$ to $s=300\ S$. Also shown are fast-Fourier transform plots of $\delta R_b(s)$ where averages are (g) from $s=0$ to $s=100\ S$, and (h) from $s=0$ to $s=300\ S$.

Downloaded 30 Aug 2001 to 192.55.106.156. Redistribution subject to AIP license or copyright, see http://ojps.aip.org/pop/popcr.jsp

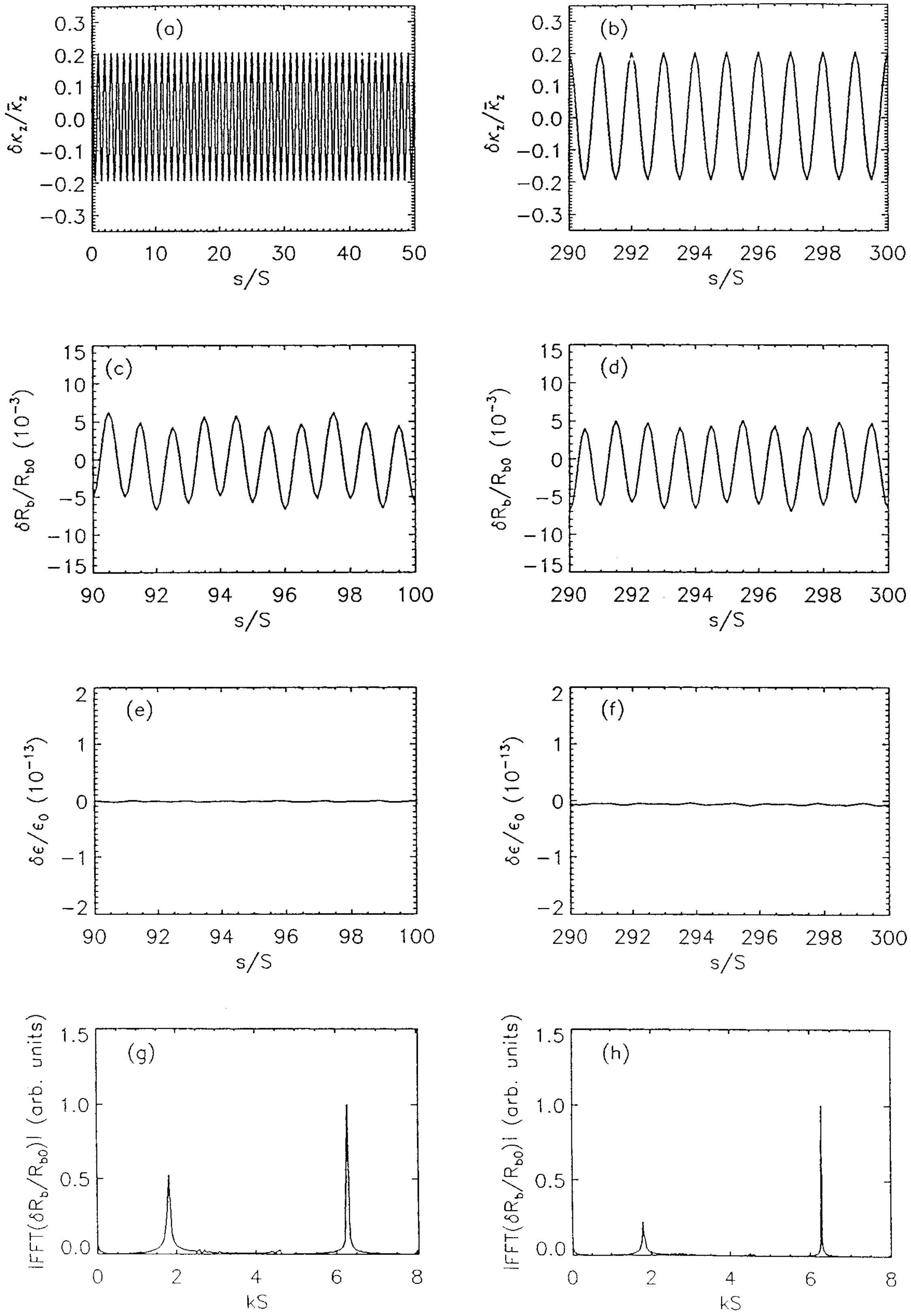

FIG. 5. Nonlinear δF-simulation results for sudden turn-on of $\delta\kappa_z(s)$ with $\alpha=\infty$ and $\Delta_m=0.2$, and normalized beam intensity $KS/\epsilon_0=0.5$. Beam propagation is from $s=0$ to $s=300\,S$, and perturbations are about the thermal equilibrium distribution $F_b^0(H_\perp)$ in Eq. (23). Shown are plots vs s/S of (a) $\delta\kappa_z(s)/\overline{\kappa_z}$ from $s=0$ to $s=50\,S$; (b) $\delta\kappa_z(s)/\overline{\kappa_z}$ from $s=290\,S$ to $s=300\,S$; (c) $\delta R_b(s)/R_{b0}$ from $s=90\,S$ to $s=100\,S$; (d) $\delta R_b(s)/R_{b0}$ from $s=290\,S$ to $s=300\,S$; (e) $\delta\epsilon(s)/\epsilon_0$ from $s=90\,S$ to $s=100\,S$; and (f) $\delta\epsilon(s)/\epsilon_0$ from $s=290\,S$ to $s=300\,S$. Also shown are fast-Fourier transform plots of $\delta R_b(s)$ where averages are (g) from $s=0$ to $s=100\,S$, and (h) from $s=0$ to $s=300\,S$.

Downloaded 30 Aug 2001 to 192.55.106.156. Redistribution subject to AIP license or copyright, see http://ojps.aip.org/pop/popcr.jsp

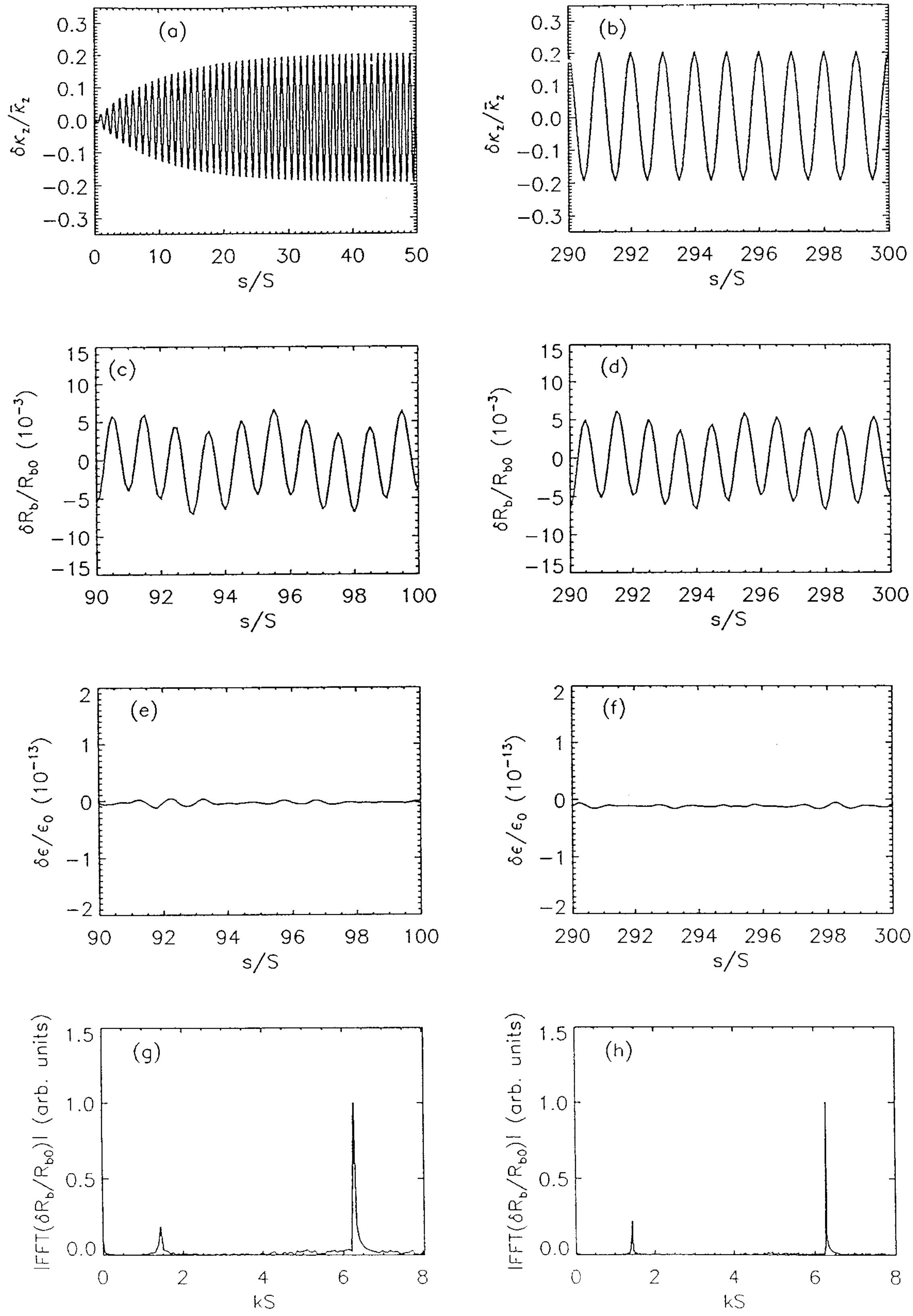

FIG. 6. Nonlinear δF-simulation results for adiabatic turn-on of $\delta\kappa_z(s)$ with $\alpha=0.1$ and $\Delta_m=0.2$, and normalized beam intensity $KS/\epsilon_0=5$. Beam propagation is from $s=0$ to $s=300\,S$, and perturbations are about the thermal equilibrium distribution $F_b^0(H_\perp)$ in Eq. (23). Shown are plots vs s/S of (a) $\delta\kappa_z(s)/\overline{\kappa_z}$ from $s=0$ to $s=50\,S$; (b) $\delta\kappa_z(s)/\overline{\kappa_z}$ from $s=290\,S$ to $s=300\,S$; (c) $\delta R_b(s)/R_{b0}$ from $s=90\,S$ to $s=100\,S$; (d) $\delta R_b(s)/R_{b0}$ from $s=290\,S$ to $s=300\,S$; (e) $\delta\epsilon(s)/\epsilon_0$ from $s=90\,S$ to $s=100\,S$; and (f) $\delta\epsilon(s)/\epsilon_0$ from $s=290\,S$ to $s=300\,S$. Also shown are fast-Fourier transform plots of $\delta R_b(s)$ where averages are (g) from $s=0$ to $s=100\,S$, and (h) from $s=0$ to $s=300\,S$.

Downloaded 30 Aug 2001 to 192.55.106.156. Redistribution subject to AIP license or copyright, see http://ojps.aip.org/pop/popcr.jsp

The initial conditions at $s=0$ for the particle positions and momenta are chosen consistently[41] with the thermal equilibrium distribution in Eq. (23). Although we do not do so here, Parker and Lee[39] have suggested a method for initializing with an arbitrary distribution, which could allow increased resolution in particularly interesting regions of the simulation, such as near the beam edge. The particle weights are chosen to be zero at $s=0$. In the δF scheme, the particle weights determine how the beam properties deviate from equilibrium. Choosing zero for the initial value of the weights implies $\delta R_b(0)=0$ and (because the thermal equilibrium distribution function is even in X' and Y'), $\delta R_b'(0)=0$. As shown in Sec. II C, these choices for $\delta R_b(0)$ and $\delta R_b'(0)$ lead to a mismatched beam for sudden turn-on of the periodic field in Eq. (31). Matching the beam by choosing $\delta R_b(0)$ and $\delta R_b'(0)$ as specified in Eq. (35) would require initializing the weights correctly, and it is not readily apparent how to accomplish this, as many choices for the initial particle weights would lead to the prescribed $\delta R_b(0)$ and $\delta R_b'(0)$. As an extreme example, one can imagine choosing all initial particle weights to be zero except for one, which is chosen by means of Eq. (41) to satisfy Eq. (35). To avoid this ambiguity, we take all initial particle weights to be zero, and instead accomplish beam matching by the adiabatic turn-on of $\delta\kappa_z(s)$.

Conservation of the total number of particles requires that the sum of the particle weights be equal to zero for all s, i.e.,

$$\langle w\rangle = \frac{1}{N_p}\sum_{i=1}^{N_p} w_i = 0. \tag{43}$$

This constraint is a useful diagnostic for testing how well the code is modeling the true beam dynamics. For the sample parameters given above, we find $\langle w_i\rangle \approx 0.001$ over a distance $s=100S$. This deviation decreases approximately linearly with decreasing time step, so the deviation is due to integration error. In δF simulations of tokamak plasmas, similar discrepancies[45] have been observed. For the results presented in this paper, we adjust for this deviation by subtracting $\langle w\rangle$ from each particle weight at the beginning of each time step, thus ensuring particle number conservation.

As a simple test case, we first present simulation results for intense beam propagation through a uniform focusing field with $\delta\kappa_z(s)=0$ and $\Delta_m=0$. Typical numerical results are presented in Figs. 2 and 3 for the choice of self-field parameter $KS_{\mathrm{eq}}/\epsilon_0=7$, and the corresponding envelope oscillation wave number determined from Eq. (33) is given by $k_e S_{\mathrm{eq}}=1.43$. Figure 2 shows phase space plots in (X,Y) and (X,X') phase space at $s=0$ and $s=500\,S_{\mathrm{eq}}$. As would be expected, for $\delta\kappa_z(s)=0$, the (stable) thermal equilibrium beam propagates quiescently over large distances with negligible change of the distribution in phase space. Shown in Fig. 3 are plots of the change in rms beam radius $\delta R_b(s)$ determined numerically from Eq. (40) [Figs. 3(a) and 3(b)], as well as a plot of the fast-Fourier transform of $\delta R_b(s)$ integrated from $s=0$ to $s=500\,S_{\mathrm{eq}}$. Evidently, the (noise-induced) oscillations in the rms beam radius remain extremely small, with $|\delta R_b/R_{b0}|\lesssim 10^{-9}$, although there is

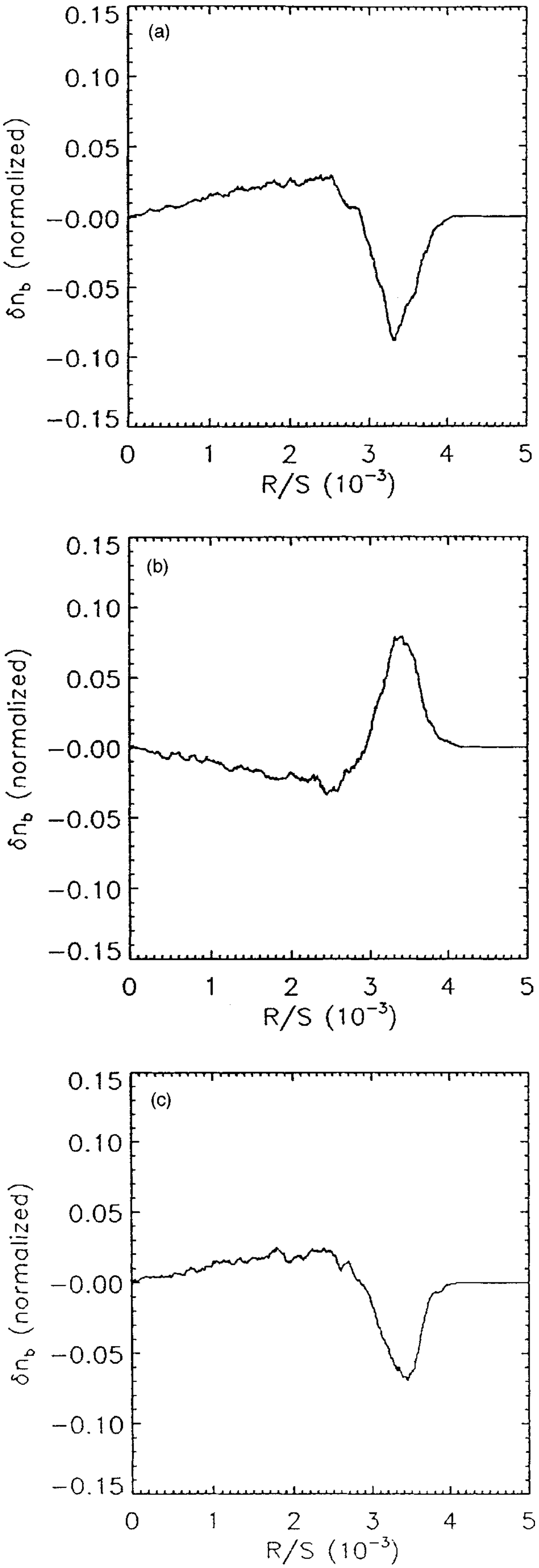

FIG. 7. Plots of the perturbed density $\delta n_b(R,s)=\int dX'\,dY'\,\delta F_b$ vs radius R obtained numerically at successive half-lattice periods corresponding to (a) $s=299\,S$, (b) $s=299.5\,S$, and (c) $s=300\,S$. System parameters in the simulation are identical to those in Fig. 6.

Downloaded 30 Aug 2001 to 192.55.106.156. Redistribution subject to AIP license or copyright, see http://ojps.aip.org/pop/popcr.jsp

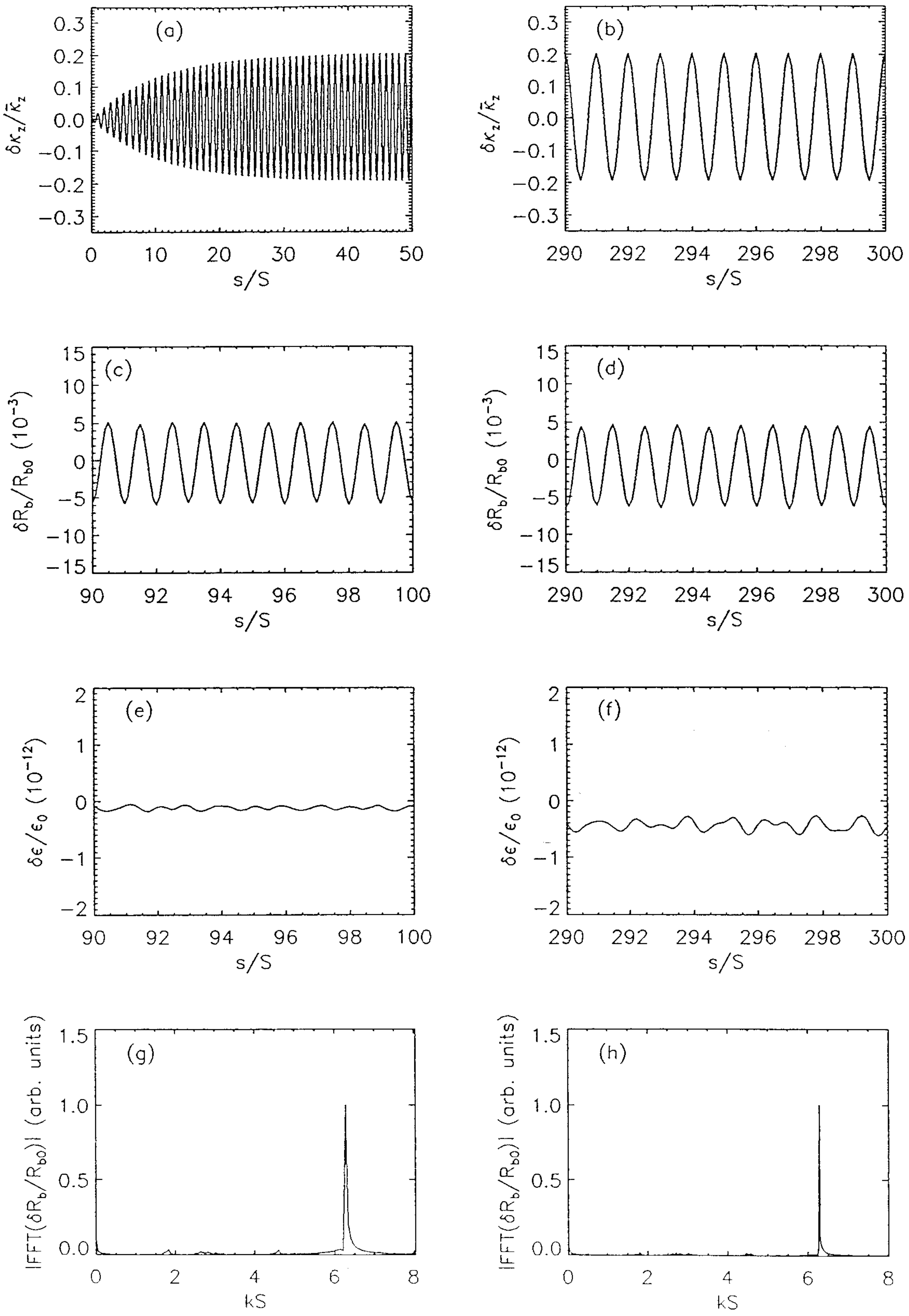

FIG. 8. Nonlinear δF-simulation results for adiabatic turn-on of $\delta\kappa_z(s)$ with $\alpha=0.1$ and $\Delta_m=0.2$, and normalized beam intensity $KS/\epsilon_0=0.5$. Beam propagation is from $s=0$ to $s=300\,S$, and perturbations are about the thermal equilibrium distribution $F_b^0(H_\perp)$ in Eq. (23). Shown are plots vs s/S of (a) $\delta\kappa_z(s)/\overline{\kappa_z}$ from $s=0$ to $s=50\,S$; (b) $\delta\kappa_z(s)/\overline{\kappa_z}$ from $s=290\,S$ to $s=300\,S$; (c) $\delta R_b(s)/R_{b0}$ from $s=90\,S$ to $s=100\,S$; (d) $\delta R_b(s)/R_{b0}$ from $s=290\,S$ to $s=300\,S$; (e) $\delta\epsilon(s)/\epsilon_0$ from $s=90\,S$ to $s=100\,S$; and (f) $\delta\epsilon(s)/\epsilon_0$ from $s=290\,S$ to $s=300\,S$. Also shown are fast-Fourier transform plots of $\delta R_b(s)$ where averages are (g) from $s=0$ to $s=100\,S$, and (h) from $s=0$ to $s=300\,S$.

Downloaded 30 Aug 2001 to 192.55.106.156. Redistribution subject to AIP license or copyright, see http://ojps.aip.org/pop/popcr.jsp

some increase in oscillation amplitude in the interval $s=450\,S_{\mathrm{eq}}$ to $s=500\,S_{\mathrm{eq}}$ [Fig. 3(b)] relative to the interval $s=0$ to $s=50\,S_{\mathrm{eq}}$ [Fig. 3(a)]. Most strikingly, the envelope oscillation wave number [Fig. 3(c)] is in excellent agreement with the predicted value k_e in Eq. (33) for $KS_{\mathrm{eq}}/\epsilon_0=7$.

Nonlinear δF-simulation results for the periodic focusing case with $\Delta_m=0.2$ are presented in Figs. 4–11, including data sets for sudden turn-on with $\alpha=\infty$ for $KS/\epsilon_0=5$ (Fig. 4) and $KS/\epsilon_0=0.5$ (Fig. 5); adiabatic turn-on with $\alpha=0.1$ for $KS/\epsilon_0=5$ (Figs. 6 and 7) and $KS/\epsilon_0=0.5$ (Figs. 8 and 9); and adiabatic turn-on with $\alpha=0.02$ for $KS/\epsilon_0=5$ (Figs. 10 and 11). All simulations presented in Figs. 4–11 are carried out for beam propagation from $s=0$ to $s=300\,S$. For purposes of comparison, Figs. 4, 5, 6, 8, and 10 display similar data sets at different system parameters. Specifically, $\delta\kappa_z(s)/\overline{\kappa_z}$ is plotted versus s/S from $s=0$ to $s=50\,S$ in frame (a), and from $S=290\,S$ to $s=300\,S$ in frame (b); $\delta R_b(s)/R_{b0}$ is plotted from $s=90\,S$ to $s=100\,S$ in frame (c), and from $s=290\,S$ to $s=300\,S$ in frame (d); $\delta\epsilon(s)/\epsilon_0$ is plotted from $s=90\,S$ to $s=100\,S$ in frame (e), and from $s=290\,S$ to $s=300\,S$ in frame (f); and the fast-Fourier transform of $\delta R_b(s)$ is plotted versus kS, with averages taken from $s=0$ to $s=100\,S$ in frame (g), and from $s=0$ to $s=300\,S$ in frame (h). Figures 7, 9, and 11 show plots of the perturbed density $\delta n_b=\int dX'\,dY'\,\delta F_b$ versus radius R determined numerically at the three axial locations corresponding to (a) $s=299\,S$, (b) $s=299.5\,S$, and (c) $s=300\,S$, respectively.

We first consider the case of sudden turn-on ($\alpha=\infty$) of $\delta\kappa_z(s)$ at high and moderate beam intensities corresponding to $KS/\epsilon_0=5$ and $KS/\epsilon_0=0.5$ in Figs. 4 and 5, respectively. In this case, as evident from Figs. 4 and 5, $\delta\kappa_z(s)$ achieves the periodic wave form in Eq. (31) instantaneously at $s=0$, and sustains this wave form from $s=0$ to $s=300\,S$. As evident from Figs. 4 and 5, the change in emittance remains extremely small over the entire propagation interval, with $|\delta\epsilon/\epsilon_0|\lesssim 10^{-14}$ in the high-intensity case [Figs. 4(e) and 4(f)], and $|\delta\epsilon/\epsilon_0|\lesssim 5\times 10^{-13}$ in the low-intensity case [Figs. 5(e) and 5(f)]. It is evident that there is also a very small (negative) dc offset of a few parts in 10^{13} that develops in Figs. 5(e) and 5(f). This offset is due to integration errors that develop in computing the weights $\{w_i\}$, and can be reduced even further by decreasing the size of the time step Δs. Most striking in Figs. 4 and 5 is the fact that sudden turn-on of $\delta\kappa_z(s)$ leads to significant beam mismatch in which the variation in the rms beam radius, $\delta R_b(s)=R_b(s)-R_{b0}$, has strong oscillatory components at both the fundamental wavelength $\lambda_s=2\pi/k_s=S$ of the periodic focusing field, and at the (longer) envelope oscillation wavelength $\lambda_e=2\pi/k_e$, where k_e is defined in Eq. (33) [see Figs. 4(c) and 4(d), and Figs. 5(c) and 5(d)]. These two wavelength components are clearly evident in the fast-Fourier transform plots of $\delta R_b(s)$ presented in Figs. 4(g) and 4(h) for $KS/\epsilon_0=5$, and in Figs. 5(g) and 5(h) for $KS/\epsilon_0=0.5$. As noted earlier in this section, because $\delta R_b(0)=0$ and $\delta R_b'(0)=0$, it is expected from Eq. (34) that $\delta R_b(s)$ will have two distinct wavelength components with moderate intensity, at wavelengths $\lambda_s=2\pi/k_s=S$ and $\lambda_e=2\pi/k_e$. As expected, the

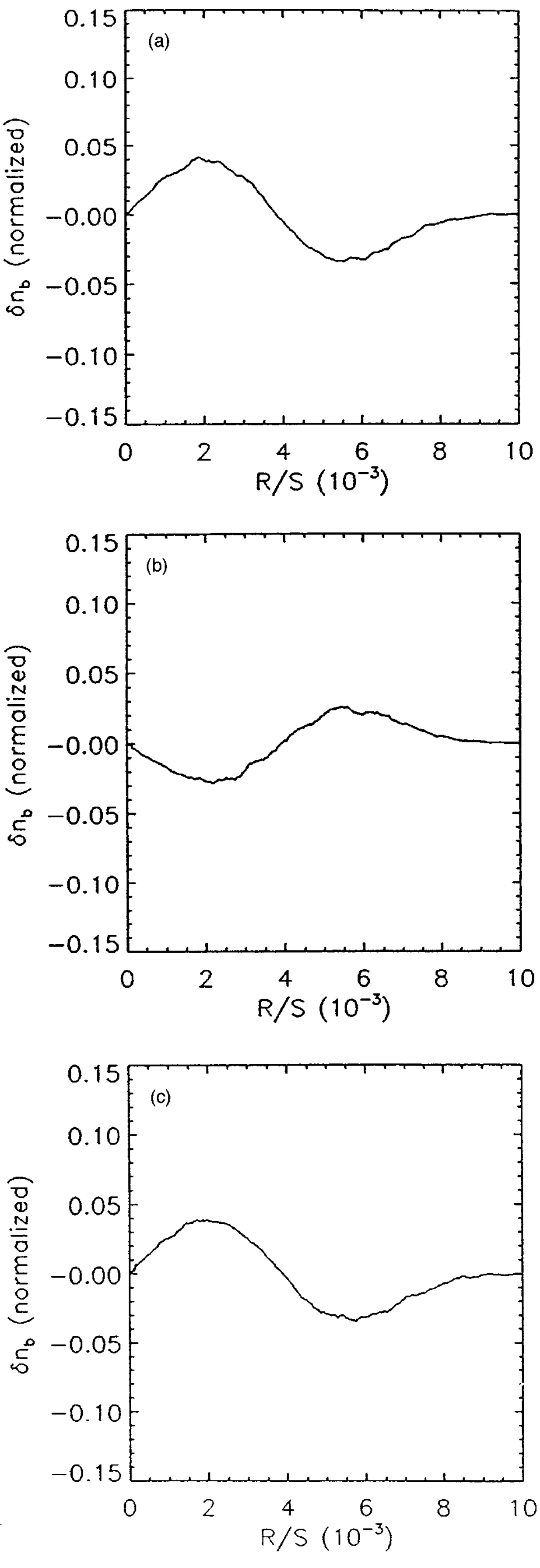

FIG. 9. Plots of the perturbed density $\delta n_b(R,s)=\int dX'\,dY'\,\delta F_b$ vs radius R obtained numerically at successive half-lattice periods corresponding to (a) $s=299\,S$, (b) $s=299.5\,S$, and (c) $s=300\,S$. System parameters in the simulation are identical to those in Fig. 8.

Downloaded 30 Aug 2001 to 192.55.106.156. Redistribution subject to AIP license or copyright, see http://ojps.aip.org/pop/popcr.jsp

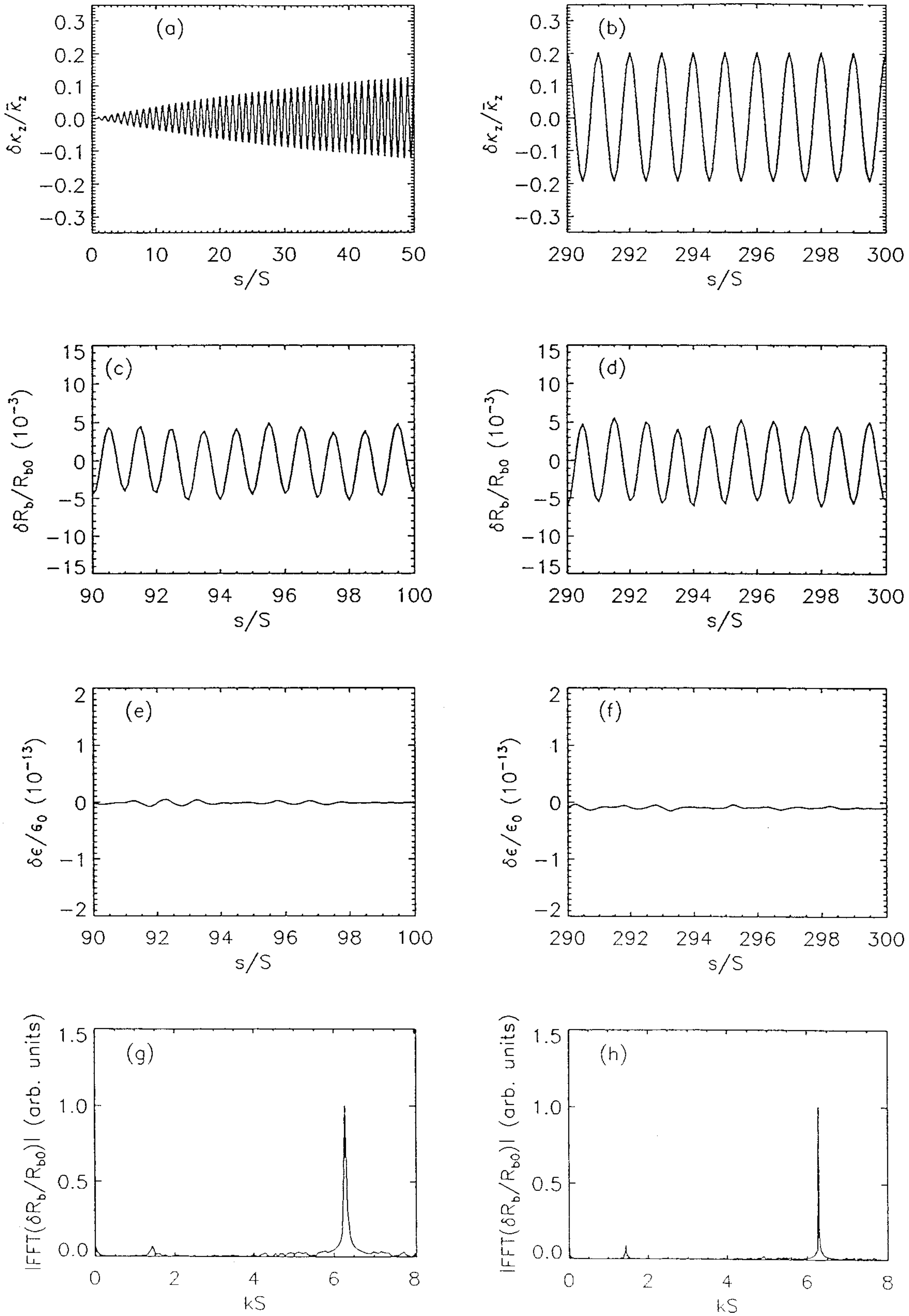

FIG. 10. Nonlinear δF-simulation results for adiabatic turn-on of $\delta\kappa_z(s)$ with $\alpha=0.02$ and $\Delta_m=0.2$, and normalized beam intensity $KS/\epsilon_0=5$. Beam propagation is from $s=0$ to $s=300\,S$, and perturbations are about the thermal equilibrium distribution $F_b^0(H_\perp)$ in Eq. (23). Shown are plots vs s/S of (a) $\delta\kappa_z(s)/\overline{\kappa_z}$ from $s=0$ to $s=50\,S$; (b) $\delta\kappa_z(s)/\overline{\kappa_z}$ from $s=290\,S$ to $s=300\,S$; (c) $\delta R_b(s)/R_{b0}$ from $s=90\,S$ to $s=100\,S$; (d) $\delta R_b(s)/R_{b0}$ from $s=290\,S$ to $s=300\,S$; (e) $\delta\epsilon(s)/\epsilon_0$ from $s=90\,S$ to $s=100\,S$; and (f) $\delta\epsilon(s)/\epsilon_0$ from $s=290\,S$ to $s=300\,S$. Also shown are fast-Fourier transform plots of $\delta R_b(s)$ where averages are (g) from $s=0$ to $s=100\,S$, and (h) from $s=0$ to $s=300\,S$.

Downloaded 30 Aug 2001 to 192.55.106.156. Redistribution subject to AIP license or copyright, see http://ojps.aip.org/pop/popcr.jsp

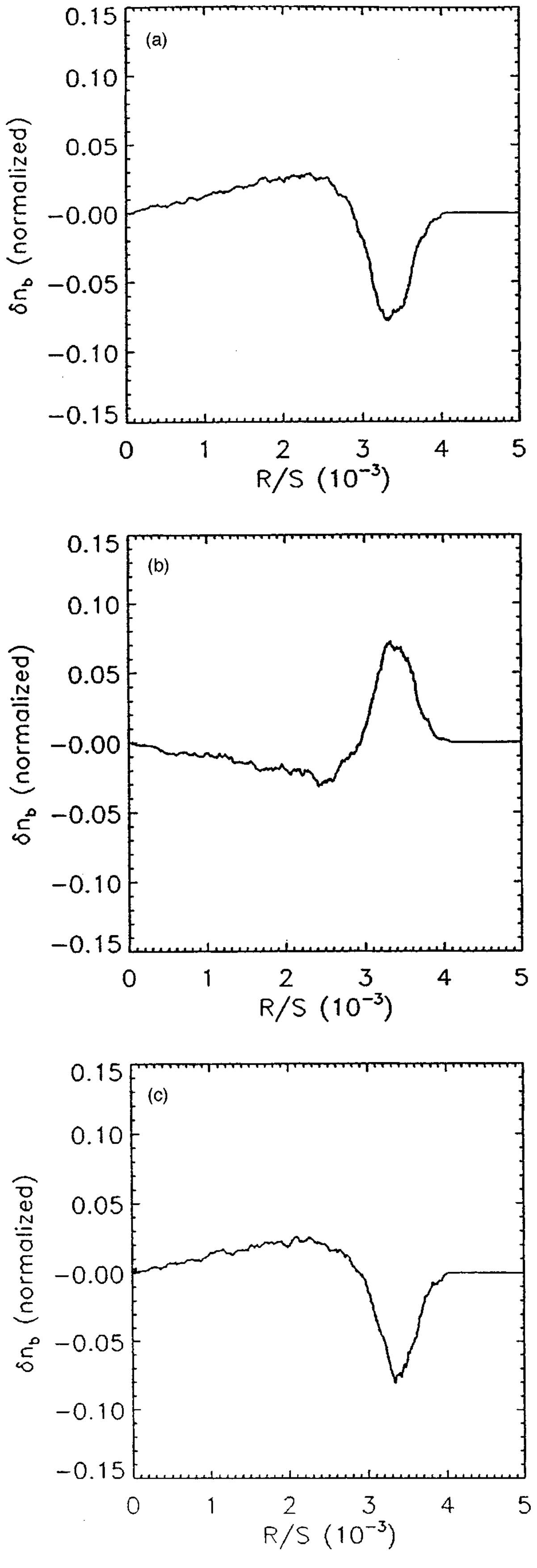

FIG. 11. Plots of the perturbed density $\delta n_b(R,s)=\int dX'\, dY'\, \delta F_b$ vs radius R obtained numerically at successive half-lattice periods corresponding to (a) $s=299\,S$, (b) $s=299.5\,S$, and (c) $s=300\,S$. System parameters in the simulation are identical to those in Fig. 10.

fast-Fourier transform peaks in Figs. 4 and 5 occur at $k_sS=2\pi$ and at the values of k_eS calculated from Eq. (33) for $KS/\epsilon_0=5$ (Fig. 4) and $KS/\epsilon_0=0.5$ (Fig. 5).

We now present nonlinear δF-simulation results for the case of adiabatic turn-on of $\delta\kappa_z(s)$. Here, the normalized field amplitude $\Delta(s)$ turns on adiabatically according to Eq. (36), with $\Delta(s)$ asymptoting at $\Delta_m=0.2$ for $s\gg S/\alpha$. Typical numerical results are presented in Figs. 6–11 for the three cases: $\alpha=0.1$ and $KS/\epsilon_0=5$ (Figs. 6 and 7); $\alpha=0.1$ and $KS/\epsilon_0=0.5$ (Figs. 8 and 9); and $\alpha=0.02$ and $KS/\epsilon_0=5$ (Figs. 10 and 11). We first note from Figs. 6 and 8, for $\alpha=0.1$, that it takes about 20 lattice periods for $\delta\kappa_z(s)$ to achieve the steady wave form in Eq. (31), whereas from Fig. 10, for $\alpha=0.02$, a steady wave form is achieved in about 100 lattice periods. Several features of Figs. 6, 8, and 10 are qualitatively similar to Figs. 4 and 5. Most notably, the change in emittance, $\delta\epsilon(s)/\epsilon_0$, remains extremely small over the entire propagation distance of 300 S. A striking difference is the effect of adiabatic turn-on in assuring *matched-beam* propagation in which the primary oscillatory component of $\delta R_b(s)$ is at the wavelength $\lambda_s=2\pi/k_s=S$ of the periodic focusing field $\delta\kappa_z(s)$. For example, at moderate beam intensity with $KS/\epsilon_0=0.5$, it follows from Figs. 8(c), 8(d), 8(g), and 8(h) that the beam is highly matched even for adiabatic turn-on parameter $\alpha=0.1$. In this case, the oscillatory component of $\delta R_b(s)$ at wavelength $\lambda_e=2\pi/k_e$ is negligibly small in comparison with the oscillation at wavelength $\lambda_s=S$. On the other hand, at high beam intensity with $KS/\epsilon_0=5$, for $\alpha=0.1$, it is clear from Figs. 6(c), 6(d), 6(g) and 6(h) that a moderately strong envelope oscillation at wavelength $\lambda_e=2\pi/k_e$ still persists, although it is greatly reduced in intensity relative to the sudden turn-on case in Fig. 4. However, for $KS/\epsilon_0=5$ and even slower adiabatic turn-on corresponding to $\alpha=0.02$ in Fig. 10, it is clear from Figs. 10(c), 10(d), 10(g), and 10(h) that the beam is highly matched in the high-intensity case. We conclude from the simulation results presented in Figs. 4, 5, 6, 8, and 10 that adiabatic turn-on of $\delta\kappa_z(s)$ is a powerful technique for beam matching.

Finally, Figs. 7, 9, and 11 show plots of the perturbed density $\delta n_b(R,s)=\int dX'\, dY'\, \delta F_b$ versus radius R determined numerically at the three axial locations corresponding to (a) $s=299\,S$, (b) $s=299.5\,S$, and (c) $s=300\,S$, respectively. The results in Figs. 7, 9, and 11 correspond to the system parameters and nonlinear δF simulations presented in Figs. 6, 8, and 10, respectively. As expected, from Figs. 7, 9, and 11, $\delta n_b(R,s)$ has regions of positive and negative perturbed density over the radial extent of the beam. Moreover, in the high-intensity case ($KS/\epsilon_0=5$ in Figs. 7 and 11), where the equilibrium density profile $n_b^0(R)$ falls off rather abruptly near the outer edge of the beam (see Fig. 1), the density perturbation $\delta n_b(R,S)$ is largely concentrated in this outer region. By contrast, at moderate beam intensity ($KS/\epsilon_0=0.5$ in Fig. 9), the equilibrium density profile $n_b^0(R)$ is radially more diffuse and bell-shaped (see Fig. 1), and the density perturbation $\delta n_b(R,s)$ extends throughout the beam, as expected. A striking feature of Figs. 7, 9, and 11 is that $\delta n_b(R,s)$ exhibits oscillatory behavior with period k_s

Downloaded 30 Aug 2001 to 192.55.106.156. Redistribution subject to AIP license or copyright, see http://ojps.aip.org/pop/popcr.jsp

$=2\pi/k_s=S$ corresponding to that of the periodic focusing field.

IV. CONCLUSIONS

In this paper, we have developed and applied the nonlinear δF formalism for intense non-neutral beam propagation through a periodic focusing solenoidal field $\kappa_z(s+S)=\kappa_z(s)$. Following a description of the theoretical model (Sec. I), the δF formalism was developed (Sec. II) by dividing the total distribution F_b into a zero-order part (F_b^0) that propagates through the average focusing field $\overline{\kappa_z}=\text{const}$, plus a perturbation (δF_b) which evolves nonlinearly in the zero-order and perturbed field configurations, including the effects of the oscillatory component of the focusing field, $\delta\kappa_z(s)=\kappa_z(s)-\overline{\kappa_z}$. Assuming perturbations about a thermal equilibrium distribution F_b^0, nonlinear δF-simulation results were presented (Sec. III) for a wide range of beam intensities as measured by the dimensionless parameter KS/ϵ_0. Adiabatic turn-on of $\delta\kappa_z(s)$ over 20–100 lattice periods was found to produce a highly matched, periodically focused beam in which the rms beam radius $R_b(s)$ oscillates with the same period S as the focusing field. Quiescent, matched-beam propagation at moderate-to-high beam intensities was demonstrated over several hundred lattice periods (300 S) in the present simulations. Most strikingly, following adiabatic turn-on, the simulations showed that $F_b=F_b^0+\delta F_b$ corresponds to a periodically focused beam equilibrium that propagates quiescently over large distances. This is a significant result because there are *no known analytical solutions* for a periodically focused thermal equilibrium beam at high beam intensities, although such a solution is clearly accessed in the simulations.

The nonlinear δF formalism developed in Sec. II is applicable to a wide range of choices of equilibrium distribution $F_b^0(H_\perp)$ and perturbations with both azimuthal and radial variation. Future applications of the nonlinear δF-simulation technique will include: (a) extension to the case where the perturbations δF_b and $\delta\psi$ are allowed to have azimuthal variations $(\partial/\partial\Theta\neq 0)$, and (b) investigations of stability behavior for other choices of equilibrium distribution $F_b^0(H_\perp)$, e.g., the Gaussian inverted-population distribution in Eq. (24).

As a final point regarding the theoretical model, we emphasize that the nonlinear δF formalism developed here is particularly well-suited for application to a periodic focusing solenoidal lattice, $\kappa_z(s)=\overline{\kappa_z}+\delta\kappa_z(s)$, in which case the average lattice coefficient $\overline{\kappa_z}=S^{-1}\int_{s_0}^{s_0+S}ds\,\kappa_z(s)$ is manifestly nonzero [see Eqs. (1) and (31)] and provides transverse confinement of the beam particles making up the equilibrium distribution $F_b^0(H_\perp)$. For adiabatic turn-on of $\delta\kappa_z(s)$, quiescent, highly matched beam propagation at moderate-to-high beam intensity has been demonstrated for propagation of a thermal equilibrium beam over hundreds of lattice periods (see, e.g., Figs. 8 and 10). For periodic focusing quadrupole systems, however, it follows that $S^{-1}\int_{s_0}^{s_0+S}ds\,\kappa_q(s)=0$, and alternative averaging techniques are required to apply the nonlinear δF formalism to high-intensity matched-beam propagation. In this regard, one promising approach for a periodic quadrupole lattice is to first carry out a Floquet transformation[43,44] to incorporate the average effects of the focusing field. This and other approaches are currently under development by the authors for application of the nonlinear δF formalism to periodic quadrupole transport systems.

Finally, it should be pointed out that parametric resonances and chaotic particle motion often play an important role in the nonlinear dynamics of space-charge-dominated beams, particularly for the case of mismatched beams (see, e.g., Ref. 44). While the present nonlinear δF formalism incorporates such effects self-consistently when they occur, no evidence for parametric instabilities was observed in the matched-beam simulations presented here, at least for the case of a thermal equilibrium distribution $F_b^0(H_\perp)$ and the range of values of phase advance ($\sigma_v=57.3°$, and σ ranging from 11° to 44.7°) considered in the present analysis.

ACKNOWLEDGMENTS

The authors thank Mobola Campbell and Hong Qin for proofreading the manuscript. This research was supported by the U.S. Department of Energy, and by the APT Project and the LANSCE Division of the Los Alamos National Laboratory.

[1] R. C. Davidson, *Physics of Nonneutral Plasmas* (Addison–Wesley, Reading, MA, 1990), Chap. 10, and references therein.

[2] T. P. Wangler, *Principles of RF Linear Accelerators* (Wiley, New York, 1998).

[3] M. Reiser, *Theory and Design of Charged Particle Beams* (Wiley, New York, 1994).

[4] D. A. Edwards and M. J. Syphers, *An Introduction to the Physics of High-Energy Accelerators* (Wiley, New York, 1993).

[5] I. Kapchinskij and V. Vladimirskij, in *Proceedings of the International Conference on High Energy Accelerators and Instrumentation* (CERN Scientific Information Service, Geneva, 1959), p. 274.

[6] R. Gluckstern, in *Proceedings of the 1970 Proton Linear Accelerator Conference, Batavia, IL*, edited by M. R. Tracy (National Accelerator Laboratory, Batavia, IL, 1971).

[7] H. Uhm and R. Davidson, Part. Accel. **11**, 65 (1980).

[8] I. Hofmann, L. Laslett, L. Smith, and I. Haber, Part. Accel. **13**, 145 (1983).

[9] J. Struckmeier, J. Klabunde, and M. Reiser, Part. Accel. **15**, 47 (1984).

[10] E. P. Lee, Nucl. Instrum. Methods Phys. Res. A **15**, 576 (1987).

[11] F. Guy, P. Lapostolle, and T. Wangler, in *Proceedings of the 1987 Particle-Accelerator Conference*, edited by E. R. Lindstrom and L. S. Taylor (Institute of Electrical and Electronic Engineering Piscataway, NJ, 1987), p. 1149.

[12] D. Neuffer, E. Colton, D. Fitzgerald, T. Hardek, R. Hutson, R. Macek, M. Plum, H. Thiessen, and T.-S. Wang, Nucl. Instrum. Methods Phys. Res. A **321**, 1 (1992).

[13] Q. Qian, R. C. Davidson, and C. Chen, Phys. Rev. E **51**, 5216 (1995).

[14] Q. Qian, R. C. Davidson, and C. Chen, Phys. Plasmas **2**, 2674 (1995).

[15] Q. Qian and R. C. Davidson, Phys. Rev. E **53**, 5349 (1996).

[16] C. Chen, Q. Qian, and R. C. Davidson, Fusion Eng. Des. **32**, 159 (1996).

[17] R. L. Gluckstern, W.-H. Cheng, S. S. Kurennoy, and H. Ye, Phys. Rev. E **54**, 6788 (1996).

[18] R. L. Gluckstern, Phys. Rev. Lett. **73**, 1247 (1994).

[19] N. Brown and M. Reiser, Phys. Plasmas **2**, 965 (1995).

[20] C. Chen, R. Pakter, and R. C. Davidson, Phys. Rev. Lett. **79**, 225 (1997).

[21] R. C. Davidson and C. Chen, Part. Accel. **59**, 175 (1998).

[22] R. C. Davidson, W. W. Lee, and P. Stoltz, Phys. Plasmas **5**, 279 (1998).

[23] C. Chen and R. C. Davidson, Phys. Rev. Lett. **72**, 2195 (1994).

[24] M. Reiser, C. R. Chang, D. Kehne, K. Low, T. Shea, H. Rudd, and I. Haber, Phys. Rev. Lett. **61**, 2933 (1988).

[25] I. Hoffman and J. Struckmeier, Part. Accel. **21**, 69 (1987).

[26] J. Struckmeier and I. Hofmann, Part. Accel. **39**, 219 (1992).

Downloaded 30 Aug 2001 to 192.55.106.156. Redistribution subject to AIP license or copyright, see http://ojps.aip.org/pop/popcr.jsp

[27] I. Haber, D. A. Callahan, A. Friedman, D. P. Grote, and A. B. Langdon, Fusion Eng. Des. **32**, 159 (1996).
[28] A. Friedman and D. P. Grote, Phys. Fluids B **4**, 2203 (1992).
[29] W. W. Lee, Q. Qian, and R. C. Davidson, Phys. Lett. A **230**, 347 (1997).
[30] Q. Qian, W. W. Lee, and R. C. Davidson, Phys. Plasmas **4**, 1915 (1997).
[31] E. P. Lee and J. Hovingh, Fusion Technol. **15**, 369 (1989).
[32] R. A. Jameson, in *Advanced Accelerator Concepts*, edited by J. S. Wurtele [AIP Conf. Proc. **279**, 969 (1993)].
[33] R. W. Müller, in *Nuclear Fusion by Inertial Confinement: A Comprehensive Treatise*, edited by G. Velarde, Y. Ronen, and J. M. Martinez-Val (CRC Press, Boca Raton, FL, 1993), Chap. 17, pp. 437–453.
[34] See, e.g., *Proceedings of the 1995 International Symposium on Heavy Ion Inertial Fusion*, edited by J. J. Barnard, T. J. Fessenden, and E. P. Lee [Fusion Eng. Des. **32**, 1 (1996)], and references therein.
[35] A. Friedman, R. O. Bangerter, and W. B. Hermannsfeldt, in *Proceedings of the IAEA Technical Committee Meeting on Drivers for Inertial Confinement Fusion, Paris, France, 1994* (Commisariat a l'Energie Atomique, Saclay, France, 1995), p. 243.
[36] E. P. Lee and R. K. Cooper, Part. Accel. **7**, 83 (1976).
[37] E. P. Lee and R. J. Briggs, LBNL Report No. 40774 (1997).
[38] A. M. Dimits and W. W. Lee, J. Comput. Phys. **107**, 309 (1993).
[39] S. E. Parker and W. W. Lee, Phys. Fluids B **5**, 77 (1993).
[40] G. Hu and J. A. Krommes, Phys. Plasmas **1**, 863 (1994).
[41] P. H. Stoltz, W. W. Lee, and R. C. Davidson, Nucl. Instrum. Methods Phys. Res. **415**, 433 (1998).
[42] See, e.g., Ref. 1, Chaps. 4 and 9.
[43] S. Y. Lee and A. Riabko, Phys. Rev. E **51**, 1609 (1995).
[44] A. Riabko, M. Ellison, X. Kang, S. Y. Lee, D. Li, J. Y. Liu, X. Pei, and L. Wang, Phys. Rev. E **51**, 3529 (1995).
[45] Z. Lin (private communication).

Downloaded 30 Aug 2001 to 192.55.106.156. Redistribution subject to AIP license or copyright, see http://ojps.aip.org/pop/popcr.jsp